MULTISCALING PROPERTIES OF CONCENTRATION FLUCTUATIONS IN DISPERSING PLUMES REVEALED USING AN ORTHONORMAL WAVELET DECOMPOSITION

EUGENE YEE
Defence Research Establishment Suffield, P.O. Box 4000, Medicine Hat, Alberta, T1A 8K6 Canada

R. CHAN and P. R. KOSTENIUK
Kosteniuk Consulting Ltd, #21-719 10th Street East, Saskatoon, Saskatchewan, S7K 0H2 Canada

C. A. BILTOFT and J. F. BOWERS
Meteorology Division, West Desert Test Center, U.S. Army Dugway Proving Ground, Dugway, Utah 84022–5000, USA

(Received in final form 19 September, 1995)

Abstract. The dynamical characteristics of concentration fluctuations in a dispersing plume over the energetic and inertial-convective range of scales of turbulent motion are studied using a multiscale analysis technique that is based on an orthonormal wavelet representation. It is shown that the Haar wavelet concentration spectrum is similar to the Fourier concentration spectrum in that both spectra exhibit an extensive inertial-convective subrange spanning about two decades in frequency, with a scaling exponent of $-5/3$. Analysis of the statistical properties (e.g., fluctuation intensity, skewness, and kurtosis) of the concentration wavelet coefficients (i.e., the concentration discrete detailed signal) suggests that the small scales are always more intermittent than the large scales. The degree of intermittency increases monotonically with decreasing scale within the inertial-convective subrange, reaching a plateau at the very small scales associated with the beginning of the near-dissipation subrange. The probability density function (pdf) of the concentration discrete detailed signal displays stretched exponential tails with an intermittency exponent (tail slope) q that increases as τ^a, where τ is the scale or dilation and a is a power-law exponent that is dependent on downwind distance, plume height, and stratification strength with typical values in the range from about 0.25 to 0.35. It is shown that the concentration variance cascade process requires a phase coherency of eddies between different scales at the small-scale end of the inertial-convective subrange.

The variation of the concentration wavelet statistics with height above the ground is investigated. The increased mean shear near the ground smooths the fine-scale plume structure for scales within the inertial-convective subrange, producing a weaker spatiotemporal intermittency in the concentration field compared to that measured higher up in the plume. The pdf of the concentration detailed signal at a fixed scale possesses less elongated tails with decreasing height z. The intermittency exponent q is found to decrease roughly linearly with increasing z.

Finally, the results of the wavelet decomposition are combined to provide a conceptual model of the turbulent transport, stirring, and mixing regimes in a dispersing plume. The implications of the results for contaminant texture in a plume are discussed.

1. Introduction

The dispersion of contaminant material in the atmospheric boundary layer is dependent on a continuous spectrum of interacting turbulent motions imposed by the background velocity field. The turbulent velocity generates high levels of variability in plume concentrations over a large range of scales and, indeed, the source

Boundary-Layer Meteorology **77:** 173–207, 1996.

size and the evolving width of the instantaneous plume introduce additional length scales that interact with the scales of the hydrodynamic field. A major obstacle to the study of the atmospheric dispersion of a scalar in a turbulent plume or jet is the lack of an exact or rigorous theory of turbulent diffusion owing to our poor understanding of the nonlinear interactions between the large number of scales of motion involved. At present, the intrinsic nature of the phenomenon is too complex to be adequately described. Nevertheless, an understanding of the spatiotemporal structure of turbulent plumes, clouds, jets, wakes, and mixing layers is essential for a variety of applications. These include atmospheric microstructural transport and dilution (e.g., prediction of the spatiotemporal distribution of a contaminant substance in an environmental flow), problems related to the effectiveness of turbulent combustion and chemical reactions in many industrial and environmental processes (e.g., formation of acid rain, NO_x, etc.), effects of a turbulent atmosphere on the propagation of electromagnetic and acoustic waves, and a plethora of more specific subjects that requires a knowledge of the detailed structure of mixing layers, wakes, jets, plumes and clouds.

Because of these important and diverse practical applications, a number of empirical and observational programs for the measurement of concentration fluctuations in dispersing clouds and plumes has been undertaken in recent years. These experimental investigations include both laboratory and full-scale field studies. Warhaft (1984) and Stapountzis *et al.* (1986) investigated line source dispersion in decaying grid turbulence in a wind tunnel; Fackrell and Robins (1982) and Bara *et al.* (1992) studied point source dispersion in a turbulent, neutrally stable boundary-layer in a wind tunnel and water channel, respectively; and, Deardorff and Willis (1984) made measurements of concentration fluctuations in buoyant and non-buoyant plumes under convective conditions in a water tank. In conjunction with these studies, a number of full-scale atmospheric measurements of concentration fluctuations in plumes and clouds has been made under a variety of meteorological conditions ranging from convective to extremely stable stratification (e.g., Hanna, 1984; Sawford *et al.*, 1985; Dinar *et al.*, 1988; Peterson *et al.*, 1990; Mylne and Mason, 1991; Mylne, 1993; Yee *et al.*, 1993, 1994a,b, 1995). Most of these studies have concentrated on providing a purely statistical description of concentration fluctuations. This analysis is usually based on a number of descriptive statistics such as various higher-order moments (e.g., fluctuation intensity, skewness, kurtosis, etc.) of the fluctuating concentration. Frequently, the latter information is summarized in terms of a concentration probability distribution that combines all the statistical moments into a single function. This phenomenological approach to concentration fluctuation research is necessary because no comprehensive theory of turbulent diffusion exists at present; and, it is anticipated that this area of investigation will remain largely empirical for some time to come.

This is not too surprising because turbulent diffusion in real flows (e.g., non-stationary and inhomogeneous turbulent flows such as those in the atmospheric boundary layer) is an extremely complex nonlinear dissipative dynamical pro-

cess that involves a tremendous range of spatial and temporal scales between the large eddies (at which concentration variance is produced) and the small eddies (at which concentration variance is dissipated). It is the enormous range of scales and nonlinearity of the interactions between scales that make the measurement, interpretation, and modeling of concentration fluctuations in dispersing plumes extremely difficult. In consequence, most of the analyses of concentration fluctuation data have focussed on a gross statistical description of the phenomenon based on a number of concentration moments, often with the implicit understanding that these techniques are insufficient to describe accurately its fundamental aspects. More recently, a spectral description of concentration fluctuations based on the Fourier transform has provided some valuable information on the dominant (energy-containing) time and space scales of motion in a dispersing plume (Hanna and Insley, 1989; Mylne and Mason, 1991; Yee *et al.*, 1993, 1994a, 1995). However, conventional spectral analysis discards detailed phase information and, as a consequence, is rather limited in that it does not allow identification of the position (or time) of occurrence and characteristic scale of the concentration events that provided the principal contributions to the observed global statistical plume properties. The latter information would be very useful for obtaining physical insights into the kinematics and dynamics of the fluctuation phenomenon, a necessary ingredient if we are to develop models of concentration fluctuations that incorporate greater physical reality.

In view of the large hierarchy of eddy sizes (scales) that is responsible for the observed fluctuating concentration, it would be instructive to apply a multiscale analysis to concentration fluctuation data. This form of analysis allows the various physical space structures at each eddy size (scale) that contribute to the fluctuating concentration to be isolated and studied. Hopefully, this approach would lead to a more detailed understanding of the interaction of the various time and space scales that produce the fluctuating concentration, as well as the dynamics of the concentration variance cascade process that transfers fluctuation variance (energy) from the large scales to the small scales. The principal objective of the present work, then, is to apply a multi-scale or multi-resolution analysis to some concentration data based on an orthonormal wavelet representation (local transform). In view of the local and non-periodic nature of concentration eddies, a signal processing tool such as the wavelet transform that allows both a time and scale (or frequency) localization offers a convenient and natural method for the investigation of concentration fluctuations.

2. Experimental Details and the Dataset

The data for this study were collected in May 1994 during Phase IV of a cooperative Concentration Fluctuation experiment (CONFLUX) project involving defence research establishments in the United States, United Kingdom, and Canada. The

experiments were conducted over flat and homogeneous terrain near Tower Grid on U.S. Army Dugway Proving Ground, Utah (40°06′ N, 112°59′ W), about 2 km west of Camel Back Ridge on the edge of the Great Salt Lake Desert. Booms were installed at 16 levels between 0 and 16 m on the 100-m high tower at the site, and used to accomodate 16 fast-response concentration sensors used for measurement of the instantaneous concentration at various positions in a vertical cross-section through a dispersing plume at downwind distances ranging from 12.5 to 100 m.

The concentration sensor used was a recently developed fast-response photoionization detector (TIP-SJ2, S & J Engineering, Inc.). The response time of the detectors, obtained by measuring the rise time (5–95%) of the leading edge of a narrow pulse of gas delivered to the sampling inlet of the detector, was about 10^{-3} s. The effective detection cell length of the sensor, normal to the flow, was about 1.7 mm which should be compared to a typical Kolmogorov length scale of about 1 mm in the atmosphere. The temporal and spatial resolution of the detector allowed most of the dynamically relevant scales responsible for plume dispersion to be measured (e.g., the energetic and inertial-convective subrange fluctuations, and some of the near-dissipation subrange). The concentration detectors were operated in all the experiments at above-ground heights of 0.5, 1, 1.5, 2, 2.5, 3, 4, 5, 6, 7, 8, 9, 10, 12, 14, and 16 m on the tower. In addition, simultaneous measurements of the horizontal (u, v) and vertical (w) components of the instantaneous wind velocity were made with three-axis sonic anemometer/thermometers (model RSWS-201/3A, Applied Technologies, Inc.) at 3 and 10 m, and horizontal components of the instantaneous wind velocity were made with two-axis sonic anemometer/thermometers (model RSWS-201/2A, Applied Technologies, Inc.) at 1.5 and 16 m.

Propylene (C_3H_6) was used as the tracer; it was released continuously from a point source at various heights between 1 and 5 m. A wind vane, collocated with the source, was used to position the source in each experiment so that the vertical array of concentration detectors was situated as close as possible to the mean-plume centerline. In all the experiments, we estimated that the detector array was less than about $0.1(y/\sigma_y)$ from the mean-plume centerline, where y is the transverse distance from the mean-plume centerline as determined from the observed mean wind direction, and σ_y is the mean-plume dispersion. A detailed description of the site and instrumentation was given in Yee *et al.* (1993, 1994a). A comprehensive analysis of the statistical characteristics of plume concentration fluctuations in vertical plume profiles obtained during Phase IV of the CONFLUX project has been documented in Yee *et al.* (1995).

The data used in this study have been taken primarily from two field experiments: experiment CC05 conducted from 00:39:00 to 01:14:00 UTC on May 19, 1994, during slightly convective meteorological conditions at a downwind distance x = 50 m with a 1 m source height; and, experiment CC24 conducted from 05:10:00 to 05:45:00 UTC on May 24, 1994, under slightly stable meteorological conditions at a downwind distance x = 12.5 m with a 1 m source height. The concentration fluctuation time series obtained from these field experiments were first low-passed

TABLE I

Summary of turbulence statistics measured with a 3-axis sonic anemometer at 3 m. Here U is mean wind speed; σ_u, σ_v, and σ_w are the standard deviations of velocity fluctuations in the alongwind, crosswind, and vertical directions, respectively; u_* is friction velocity; L is the Monin–Obukhov length; ϵ is the mean rate of dissipation of turbulent kinetic energy; and z_0 is the roughness length

Trial	U (m s^{-1})	σ_u (m s^{-1})	σ_v (m s^{-1})	σ_w (m s^{-1})	u_* (m s^{-1})	L (m)	ϵ (m^2 s^{-3})	z_0 (m)
CC05	4.0	1.062	0.879	0.458	0.421	−269	0.065	0.07
CC24	5.5	1.238	0.704	0.478	0.419	147	0.085	0.015

filtered with eight-pole Butterworth filters with a corner frequency (−6 dB point) at 1000 Hz to prevent aliasing, and then digitized at a sampling frequency of 4000 Hz using a 16-bit analog-to-digital (A/D) converter (HSDAS 16, Analogic Inc.). Turbulence statistics from the two field experiments obtained from the sonic anemometer/thermometer at 3 m have been summarized in Table I.

3. Orthonormal Wavelet Transform and Wavelet Statistics

In recent years, the wavelet transform has been developed by a growing and enthusiastic community of applied mathematicians as a tool for signal analysis, synthesis, and decomposition. The continuous wavelet transform has been applied successfully to geophysical data by a number of researchers. Argoul *et al.* (1989) applied it to turbulence data in order to provide some visual evidence for the existence of the Richardson (turbulence) cascade. The transform has been used by Vergassola and Frisch (1991) to study self-similar random processes. Everson *et al.* (1990) and Farge (1992) used it to extract local scaling exponents from turbulence data. It has been applied for the identification of coherent structures or events in a sheared and heated boundary layer by Mahrt (1991), and in flows within and above a canopy by Gao and Li (1993) and Collineau and Brunet (1993). To overcome certain limitations arising from the intrinsic redundancy of representation provided by the continuous wavelet transform, an orthonormal wavelet representation that conserves the signal information has been developed and applied recently to both simulated and observed geophysical data (e.g., Yamada and Ohkitani, 1990; Yamada and Ohkitani, 1991; Meneveau, 1991; Kumar and Foufoula-Georgiou, 1993; Katul *et al.*, 1994; Hayashi, 1994).

In this section, certain aspects of the orthonormal wavelet transform that are relevant to the present study are briefly reviewed. More detailed treatments of the wavelet transform (both continuous and discrete) and wavelet-based multi-resolution (multi-scaling) analysis can be found in the excellent monographs by Daubechies (1992) and Chui (1992) to which the reader is referred for more detail.

3.1. ORTHONORMAL WAVELET TRANSFORM

Consider a signal $\chi(t)$ (e.g., the fluctuating concentration) that is uniformly sampled every δt s over a sampling time T to yield N data samples (i.e., $T = N\delta t$). Furthermore, let $N = 2^M$ where M is an integer. Because it is not possible to perform an analysis at a resolution coarser than some fixed scale determined by the sampling time T, it is convenient to scale time by T, and expand the discrete signal into an orthonormal wavelet basis as follows:

$$\chi(t_i/T) = S_M\phi(t_i/T) + \sum_{j=0}^{M-1}\sum_{k=0}^{2^j-1} W_{j,k}\psi_{j,k}(t_i/T), \tag{1}$$

where $t_i \equiv i\delta t$ ($i = 0, 1, \ldots, N-1$). Here, $\phi(t)$ is a basic scaling function that determines the gross (average) structure of the signal over the sampling time, and $\psi_{j,k}(t)$ are orthonormal wavelet basis functions. The wavelets $\psi_{j,k}(t)$ are smooth wiggly functions of scale 2^{-j} and position $k/2^j$ (measured in units of the sampling time T). These functions are constructed from binary dilations (with scale index j) and dyadic translations (with translation index k) of a single function $\psi(t)$ in accordance with the following:

$$\psi_{j,k}(t) = 2^{j/2}\psi(2^j t - k), \tag{2}$$

where $\psi(t)$ is the mother wavelet. Furthermore, $\psi(t)$ is chosen so that its translations and dilations are orthogonal to each other, i.e.,

$$\int_{\mathrm{R}} \psi_{j,k}(t)\psi_{l,m}(t)\,\mathrm{d}t = \delta_{j,l}\delta_{k,m}, \tag{3}$$

where $\delta_{j,k}$ denotes the Kronecker delta function. The wavelet coefficients $W_{j,k}$ of Equation (1) are given by

$$W_{j,k} = \int_{\mathrm{R}} \chi(t)\psi_{j,k}(t)\,\mathrm{d}t, \tag{4}$$

with the appropriate orthogonal subsampling and scaling applied for finite-duration discrete-time data (e.g., Taswell and McGill, 1994).

The wavelet decomposition of the discrete signal $\{\chi(t_i)\}_{i=0}^{N-1}$ provides a time-scale representation of the signal with scale and position given by the indices j and k, respectively. The decomposition consists of two components: (1) a discrete approximation S_M of χ at the coarsest available scale (determined by the sampling time T); and, (2) the discrete detailed signals (wavelet coefficients) $\{W_{j,k}\}_{k=0}^{2^j-1}$ at scales $2^{-j}T$ ($j = 0,1,\ldots, M-1$) that embody the information relevant for "prediction" of the detailed structure of χ. The reference signal S_M can be interpreted as a weighted global mean of $\chi(t)$ over the sampling time T. Each j-level in the discrete

detailed signal corresponds to a temporal scale (period) $\tau_j \equiv 2^{-j} N\delta t = 2^{-j} T$ s (or, equivalently, to a spatial scale $r_j = U\tau_j$ on application of Taylor's frozen turbulence hypothesis using the local mean windspeed U). Hence, the wavelet decomposition $(S_M, \{W_{j,k} : j = 0, 1, \ldots, M-1; k = 0, 1, \ldots, 2^j - 1\})$ provides a multiscale representation of χ. This representation conserves information because the wavelet decomposition has the same number of samples (N) as the original signal. Indeed, the total number of wavelet coefficients $W_{j,k}$ is

$$\sum_{j=0}^{M-1} 2^j = 2^M - 1 = N - 1,$$

which in addition to the global DC offset, S_M, leads to a conservation of information.

Obviously, a mother wavelet ψ whose discrete binary dilations and dyadic translations form an orthonormal basis set must satisfy a rather restrictive set of conditions. In the present study, we will consider only the simplest wavelet basis generated by the Haar wavelet given by $\psi(t) = I_{(0,1/2]}(t) - I_{(1/2,1]}(t)$, where

$$I_A(t) \equiv \begin{cases} 1, & \text{if } t \in A; \\ 0, & \text{otherwise,} \end{cases}$$

is the indicator function (cf. Figure 1). The scaling function $\phi(t)$, corresponding to the Haar wavelet, is the indicator function of the unit interval $(0, 1]$, viz. $\phi(t) = I_{(0,1]}(t)$. Although a series of more regular (smoother) orthogonal wavelets with compact support (i.e., they are zero everywhere outside a finite interval) and a finite number of vanishing moments can be constructed (e.g., Daubechies, 1988), we found that the results of the ensuing analysis were not particularly sensitive to the choice of the particular wavelet basis set, in agreement with the conclusions of Meneveau (1991).

3.2. WAVELET COEFFICIENT STATISTICS

At a given scale index j, all standard statistical measures can be determined for the discrete detailed signal $W_{j,k}$; for example, the wavelet coefficient standard deviation,

$$\sigma(W; j) \equiv \langle W_{j,k}^2 \rangle_k^{1/2}; \tag{5a}$$

the wavelet coefficient skewness,

$$\mathrm{Sk}(W; j) \equiv \frac{\langle W_{j,k}^3 \rangle_k}{\sigma^3(W; j)}; \tag{5b}$$

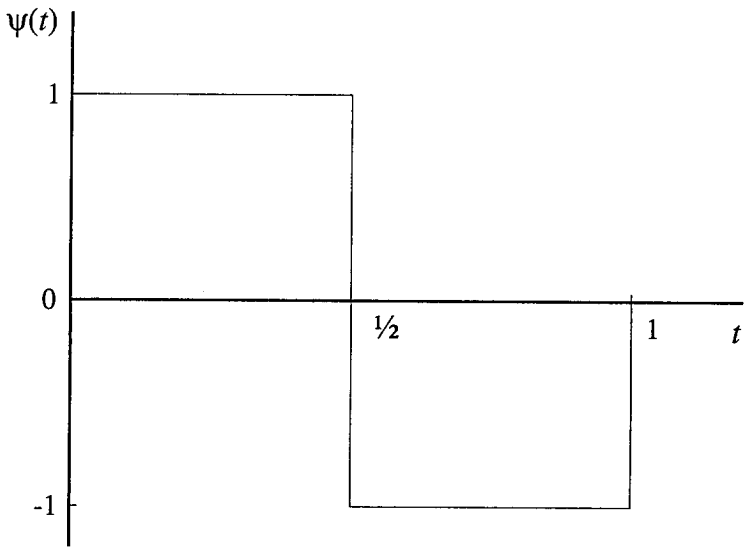

Fig. 1. The Haar wavelet function $\psi(t)$.

and the wavelet coefficient kurtosis

$$\mathrm{Ku}(W;j) \equiv \frac{\langle W_{j,k}^4 \rangle_k}{\sigma^4(W;j)}, \tag{5c}$$

at scale index j. Here $\langle \cdot \rangle_k$ denotes the time average over all time (or translation) positions (indexed by k) within the sample record at a fixed scale j.

The variance (energy) contributed by a signal event at time index k and scale index j is equal to the squared detailed component $W_{j,k}^2$. The total variance (energy) density contributed by variations with time scale τ_j (or, equivalently, with cyclic frequency $f_j \equiv \tau_j^{-1}$) is $E(f_j) = 2^j \langle W_{j,k}^2 \rangle_k / N$. The wavelet power spectral density, $\Phi(f_j)$, at frequency f_j is the energy density $E(f_j)$ per unit frequency, which can be obtained by dividing $E(f_j)$ by $\delta f_j \equiv 2^j (\delta t)^{-1} \ln 2/N$:

$$\Phi(f_j) = \langle W_{j,k}^2 \rangle_k \frac{\delta t}{\ln 2}. \tag{6}$$

We can define a number of statistical measures for the signal variance at various scales. Some examples include: the standard deviation of the signal variance at scale index j (which measures the variability of the signal energy at scale index j),

$$\sigma(W^2;j) = \frac{\delta t}{\ln 2} [\langle W_{j,k}^4 \rangle_k - \langle W_{j,k}^2 \rangle_k^2]^{1/2}; \tag{7a}$$

and non-dimensional statistics such as fluctuation intensity

$$i(W^2;j) = \frac{\sigma(W^2;j)}{\Phi(f_j)}; \tag{7b}$$

skewness

$$\mathrm{Sk}(W^2; j) = \left(\frac{\delta t}{\ln 2}\right)^3 \frac{\langle (W_{j,k}^2 - \langle W_{j,k}^2 \rangle_k)^3 \rangle_k}{\sigma^3(W^2; j)}; \tag{7c}$$

and kurtosis

$$\mathrm{Ku}(W^2; j) \equiv \left(\frac{\delta t}{\ln 2}\right)^4 \frac{\langle (W_{j,k}^2 - \langle W_{j,k}^2 \rangle_k)^4 \rangle_k}{\sigma^4(W^2; j)}; \tag{7d}$$

of signal variance (energy) at scale index j. The pair of signal variance statistics $\Phi(f_j)$ and $\Phi(f_j) + \sigma(W^2; j)$ was referred to as the "dual spectrum" by Meneveau (1991). Finally, with reference to Equation (1), the following signal variance (energy) conservation equation holds for the discrete signal:

$$\sum_{i=0}^{N-1} \chi^2(t_i/T) = S_M^2 + \sum_{j=0}^{M-1} \sum_{k=0}^{2^j-1} W_{j,k}^2. \tag{8}$$

In addition to wavelet statistics at a fixed scale, we can consider also the correlation of the instantaneous scale-conditioned signal variance $W_{j,k}^2$ between two adjacent scales. To this end, consider the following normalized signal energy variation at scale or period τ_j:

$$\beta_{j,k}^{(2)} = \frac{W_{j,k}^2}{\langle W_{j,k}^2 \rangle_k}.$$

Now, define the "correlation" $R_j^{(2)}$ of $\beta_{j,k}^{(2)}$ between two adjacent scales j and $(j + 1)$ as follows (Yamada and Ohkitani, 1991):

$$R_j^{(2)} = 2^j \sum_{k=0}^{2^{j+1}-1} \beta_{j,\lfloor k/2 \rfloor}^{(2)} \beta_{j+1,k}^{(2)}, \tag{9}$$

where $\lfloor x \rfloor$ denotes the integer part of x. Hence, $R_j^{(2)}$ is the time "correlation" of the second-order signal difference (i.e., variance or energy distribution) at two consecutive (adjacent) octaves over scales indexed by j and $(j + 1)$. Actually, $R_j^{(2)}$ is not really a true correlation coefficient in the strict sense (it is more properly interpreted as a similarity measure and, in this sense, should perhaps be more appropriately referred to as a pseudocorrelation coefficient between scales).

4. Multiscale Statistical Analysis of Concentration Data

4.1. Scale-conditioned plume concentration statistics at a fixed height

An example of a multiscale decomposition of a fluctuating concentration signal χ is shown in Figure 2. The concentration time series, taken from experiment CC05

from the detector at 1.5 m height, is shown in the top panel of Figure 2. The Haar wavelet decomposition of this signal was computed for $N = 2^M$ points with $M = 23$. The bottom panels of Figure 2 display the discrete detailed signal $W_{j,k}$ (wavelet coefficients) plotted as a function of time t for 5 different scales, namely $j = 5$, 7, 9, 11, and 13 (providing, as such, a visual indication of the irregularity of the signal at resolutions $\tau_j = 65.536$, 16.384, 4.096, 1.024, and 0.256 s for $j = 5$, 7, 9, 11, and 13, respectively).

The time series provided by the Haar wavelet coefficients $W_{j,k}$ at a fixed scale index j (cf. Figure 2) resemble the concentration increments (differences) $\Delta\chi(\tau, t) \equiv \chi(t + \tau) - \chi(t)$ over a time interval τ that is 2^{-j} times the sampling time T (i.e., $\tau = 2^{-j}T$). The basic difference is that the Haar wavelet transform (cf. Equation (4)) evaluated at scale index j (i.e., $W_{j,k}$) is equivalent to averaging $\chi(t)$ over the two half-widths defined by a dilated version of the Haar wavelet shown in Figure 1 (with dilation width $2^{-j}T$), and then computing the difference between these two means. It is noted that the latter operation partially removes the concentration variations on all time scales smaller than $2^{-j}T$ and, as such, can be interpreted as providing a band-pass filtered version of the original signal with the centre of the passing band located at the frequency $f_j \equiv \tau_j^{-1} = 2^j/T$, and a filter bandwidth Δf_j equal to one octave centred about the midband. Hence, the discrete detailed signals $W_{j,k}$ in Figure 2 can be interpreted as time records of band-pass filtered versions of the original signal with midband frequencies $f_j \equiv 2^j/T$.

From this perspective, we note that the low-frequency (or large-scale) concentration variations appear to be more space-filling in the sense that there are no quiescent parts in these variations. However, the variations at higher frequencies or smaller scales (i.e., higher scale index j) clearly exhibit more quiescent periods (e.g., note the erratic, bursting nature of the detailed signals at the smaller scales in which bursts of high turbulent activity are followed by long relatively quiescent periods). Hence, the degree of intermittency or "spottiness" in the concentration variations increases with decreasing scale, suggesting that the distribution of concentration events becomes progressively more nonuniform both temporally and spatially at the smaller scales. The spotty regions at the small scales appear to be located near sharp jumps in the original concentration signal, suggesting that sharp gradients in concentration localized at these jumps contribute directly to the observed fine-scale structure.

The degree of intermittency of the small scales can be quantified in terms of the kurtosis of $W_{j,k}$ shown in Figure 3. The latter was obtained from the concentration data shown in Figure 2. Note that the wavelet coefficient kurtosis increases with decreasing scale (or increasing frequency); it possesses a Gaussian value of 3 (approximately or better) at the large scales, and increases roughly monotonically with decreasing scale approaching a value of about 70 at a frequency of 250 Hz (or, period 0.004 s). Hence, the concentration variations become increasingly intermittent and non-Gaussian at progressively smaller scales. Here, non-Gaussianity is identified as a manifestation of intermittency, namely, that large-amplitude events

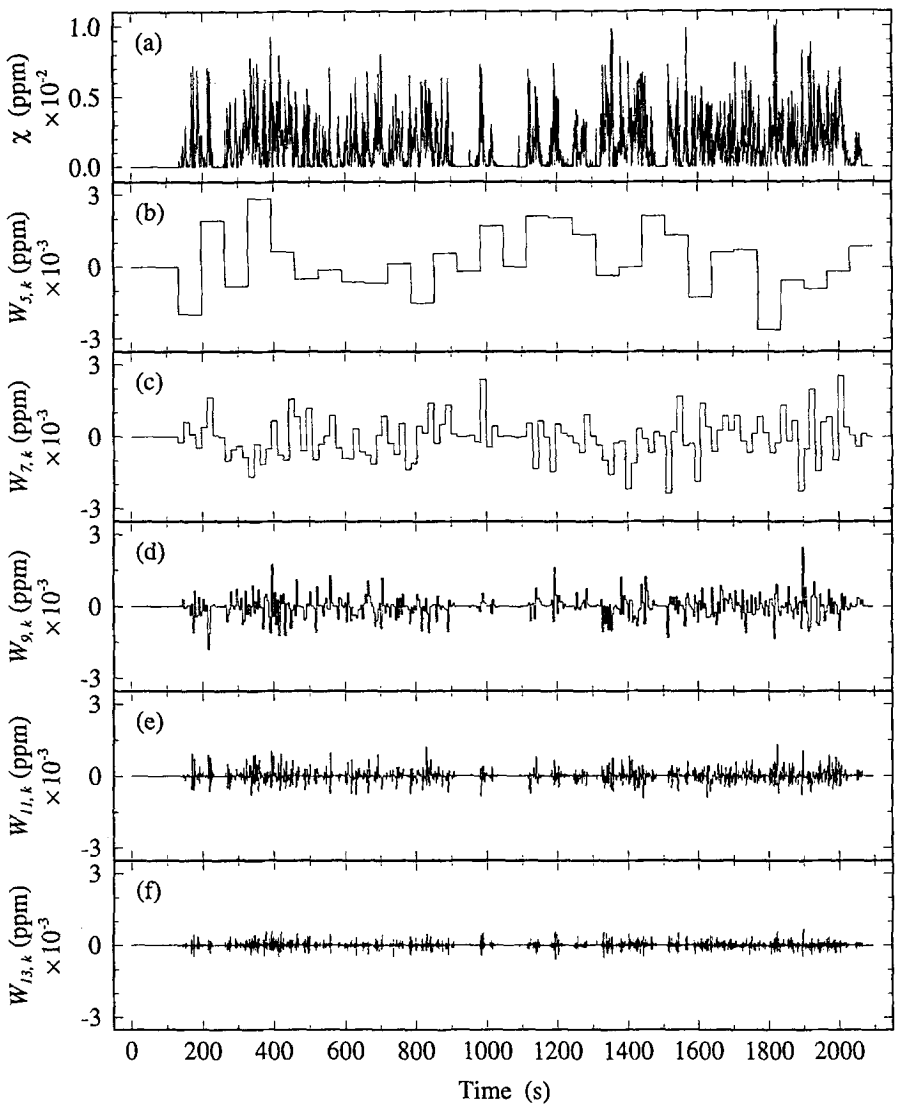

Fig. 2. Multiresolution decomposition of a fluctuating concentration time series. (a) A concentration time series taken from Trial CC05 for the detector at 1.5 m height. Discrete detailed signal, $W_{j,k}$, of concentration time series obtained from a Haar wavelet transform are shown for scale indices (b) $j = 5$; (c) $j = 7$; (d) $j = 9$; (e) $j = 11$; and, (f) $j = 13$.

occur much more frequently than in a random sample drawn from a Gaussian distribution.

Now consider the scale-dependence of the concentration variance (energy). Figure 4 shows the Haar wavelet concentration power spectrum (cf. Equation (6)) for the concentration time series shown in Figure 2. The latter spectrum is compared with that obtained from the usual Fourier basis. The spectra are plotted on a double

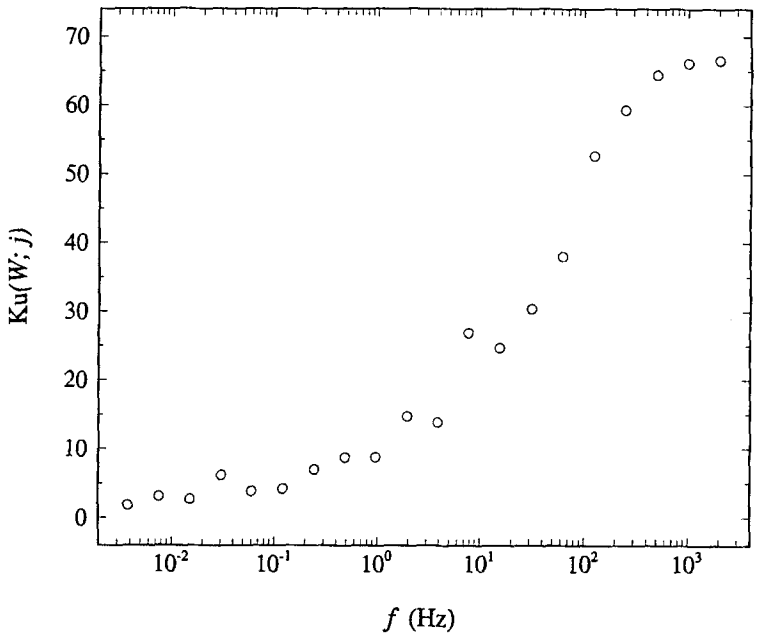

Fig. 3. Dependence of the Haar wavelet coefficient kurtosis, $\mathrm{Ku}(W; j)$, on frequency f (or, equivalently, scale index j) for the concentration time series shown in Figure 2. The frequency f corresponding to scale index j is defined as $f = f_j \equiv 2^j T^{-1}$, where T is the sampling time.

logarithmic plot with $f\Phi(f)$, normalized by the concentration variance σ_χ^2, as the ordinate. The Haar and Fourier concentration spectra have similar shapes; in particular, these two spectra agree very well at the intermediate frequencies, and the frequency of the peak of maximum fluctuation energy (variance) (which occurs at about 1 Hz) is the same for both spectra. Compared to the Fourier spectrum, the low-frequency end ($\lesssim$1 Hz) of the Haar spectrum contains more energy. Furthermore, the two spectra also differ significantly at the high-frequency (small-scale) end, where the Fourier spectrum is seen to decrease much more rapidly with increasing frequency than the Haar spectrum. Hence, there appears to be a relative shift of concentration variance to small scales in the Haar spectrum that is probably related to the local bandpass nature of the Haar wavelet transform. Both spectra exhibit the well-known $-5/3$ inertial-convective subrange (i.e., $f\Phi(f) \sim f^{-2/3}$). Deviations from the $-5/3$ scaling law in the inertial-convective subrange in the Fourier and Haar spectra are negligible, supporting the robustness of this scaling law with respect to the choice of the basis sets. The inertial-convective subrange for the Fourier spectrum extends over about 2 decades in frequency (e.g. from about 1 to 100 Hz), whereas that for the Haar spectrum extends over a larger frequency range (e.g., over about 8 octaves from $j = 11$ to 19). The shift in concentration variance to smaller scales in the Haar transform (as noted above) may explain why the $-5/3$ scaling law extends into the very small scales (e.g., toward scales smaller than

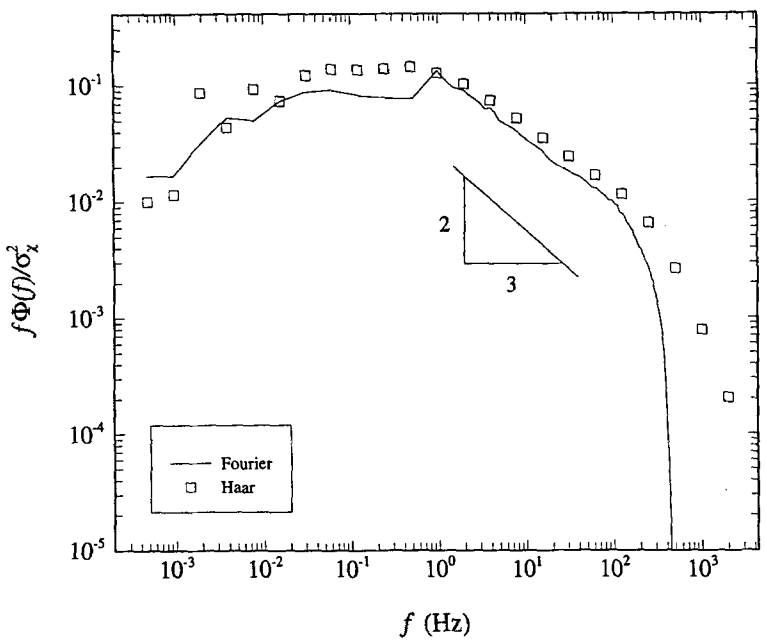

Fig. 4. Normalized Fourier and Haar wavelet concentration power spectra, $f\Phi(f)/\sigma_\chi^2$, obtained from the concentration time series shown in Figure 2. A straight line, corresponding to a slope of $-2/3$, has been included to show the extent of the inertial-convective subrange.

the Taylor microscale) that correspond to the near-dissipation range in the Fourier spectrum.

Although the robustness of the $-5/3$ scaling law over the inertial-convective subrange has been established in Figure 4, it is important to emphasize that whereas the scaling of the concentration spectrum remains constant within this range, the degree of non-Gaussianity of the concentration eddies (scales) varies significantly over this range of scales (cf. Figures 2 and 3). Figure 5 shows more clearly the variability (or the magnitude of the fluctuations) of the concentration variance (energy) with scale as embodied in various statistics extracted from the time records of $W_{j,k}^2$ (wavelet energy). Here, the scale-dependent fluctuation intensity, skewness, and kurtosis of $W_{j,k}^2$ (cf. Equations (7b), (7c), and (7d)) are displayed for the concentration data shown in Figure 2. Note that all the statistical measures of the scale-conditioned concentration variance increase with decreasing scale (or increasing frequency), suggesting an increasing "activity" in the local concentration energy at progressively smaller scales. This implies that the fluctuation variance cascade process that produces the constant $-5/3$ scaling law that is characteristic of the inertial-convective subrange (cf. Figure 4) is not statistically self-similar. In particular, the statistical law governing the turbulent cascade process is self-similar only if the probability distribution of the concentration variations is the same at

all scales, and the results of Figure 5 suggest otherwise since the measurements show that the fluctuation intensity, skewness, and kurtosis of the concentration energy increase as the resolution or scale decreases. These results suggest that the probability distribution of the concentration variations at the various scales is not self-similar, becoming progressively more non-Gaussian at smaller scales. Moreover, the fluctuation intensity of $W^2_{j,k}$ at a fixed value of j (which provides a measure of the degree of irregularity of the local concentration variance at a particular scale) is about one at the large scales, increasing to about 8 at the small scales (cf. Figure 5(a)). Hence, the local concentration variance (energy) at a particular scale can differ significantly from its mean value at that scale. At the statistical level, these results are consistent with (but do not prove) the notion that there is some cascade process (or, multiplicative effect) which transfers concentration variance from the large scales where it is produced to the small scales where it is dissipated, with the fluctuations building up as the cascade proceeds to smaller scales.

4.2. VERTICAL PROFILES OF WAVELET COEFFICIENT STATISTICS

In this section, we will explore the effect of height above the ground on the concentration wavelet coefficient statistics. To this end, a number of vertical profiles of concentration wavelet coefficient statistics for various scales will be shown, with the objective of providing some insight on the effect of increased mean shear near the ground on the statistical characteristics of fluctuating plume concentrations at each scale.

Figures 6 and 7 show the vertical profiles of the concentration variance (energy) fluctuation intensity, $i(W^2; j)$, skewness, $\mathrm{Sk}(W^2; j)$, and kurtosis, $\mathrm{Ku}(W^2; j)$, at a number of scales for Trials CC05 and CC24, respectively. These figures provide evidence of the fine-scale variability of the concentration variance cascade which transfers variance from large to small scales. In particular, at a given scale in the inertial-convective subrange (i.e., $j \lesssim 11$ corresponding to periods less than about 1 s), the concentration variance fluctuation intensity, skewness, and kurtosis roughly increase with increasing height from the ground. Furthermore, at a given height, these statistical measures increase with decreasing scale within the inertial-convective subrange. This pattern is consistent for all scales in the inertial-convective subrange at a fixed height, and for all heights in the plume at a given scale. The latter implies that at any fixed scale, the intermittency of the instantaneous concentration variance is greater at higher levels in the plume; or, at any fixed height, the level of intermittency in the local concentration variance increases as the scales decrease. In consequence, those portions of the plume near the ground appear to be more thoroughly mixed, resulting in a reduction in the irregularity or degree of intermittency in concentration variance events for all scales within the inertial-convective subrange. Variation of the concentration variance fluctuation intensity, skewness, and kurtosis with z is similar for all inertial-convective subrange scales,

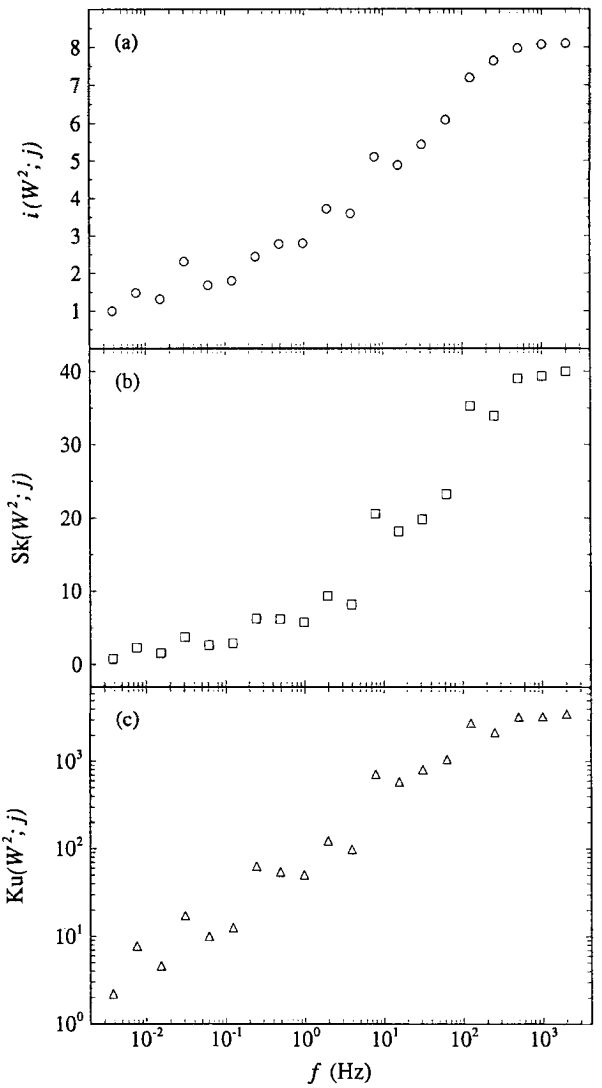

Fig. 5. Wavelet statistics of the squared discrete detailed signal $W_{j,k}^2$ versus frequency, f: (a) fluctuation intensity, $i(W^2; j)$; (b) skewness, $\mathrm{Sk}(W^2; j)$; and, (c) kurtosis, $\mathrm{Ku}(W^2; j)$. The frequency f corresponding to scale index j is defined as $f = f_j \equiv 2^j T^{-1}$, where T is the sampling time.

suggesting that the effect of the ground on mixing concentration fluctuations acts equally at all scales within this range. Moreover, it appears that scales much larger than those of the inertial-convective subrange (i.e., $j \lesssim 7$ which corresponds to periods greater than about 16 s) are not as greatly affected by the presence of the ground. The latter scales are most likely associated with the longer-term fluctuations arising from plume meandering. In summary, the small-scale turbulent

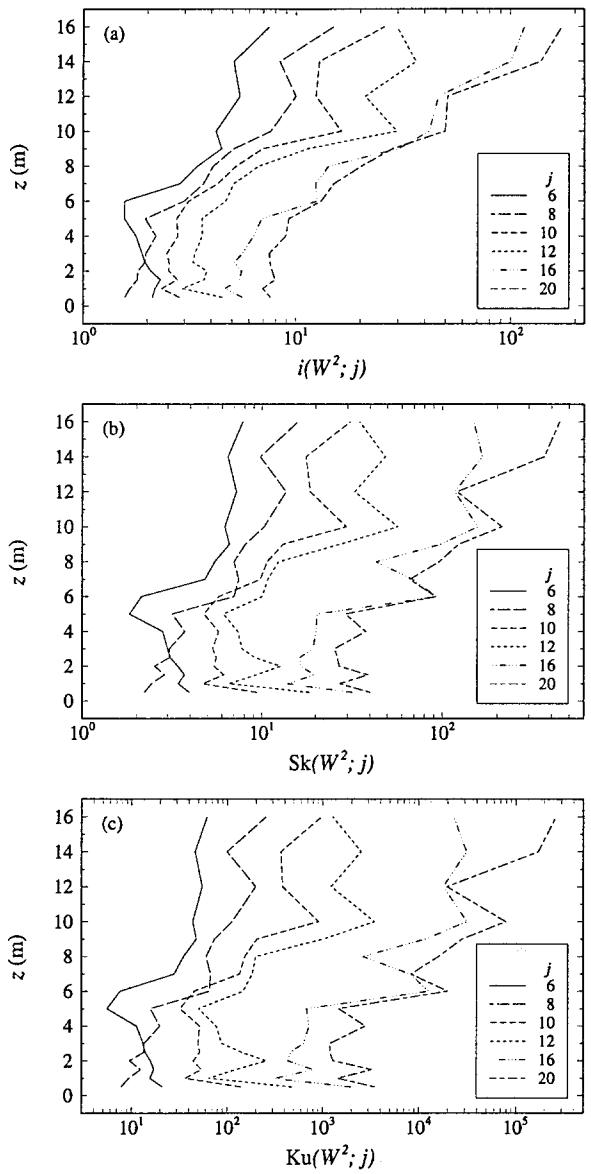

Fig. 6. Vertical profiles of wavelet statistics of the squared discrete detailed signal $W^2_{j,k}$: (a) fluctuation intensity, $i(W^2; j)$; (b) skewness, $\mathrm{Sk}(W^2; j)$; and, (c) kurtosis, $\mathrm{Ku}(W^2; j)$ for j = 6, 8, 10, 12, 16, and 20. The data were taken from Trial CC05.

velocity eddies near the ground appear to be more effective at mixing concentration fluctuations at scales in the inertial-convective subrange (associated with in-plume mixing) than they are in destroying fluctuations at the larger scales of the energetic subrange (associated with plume meandering).

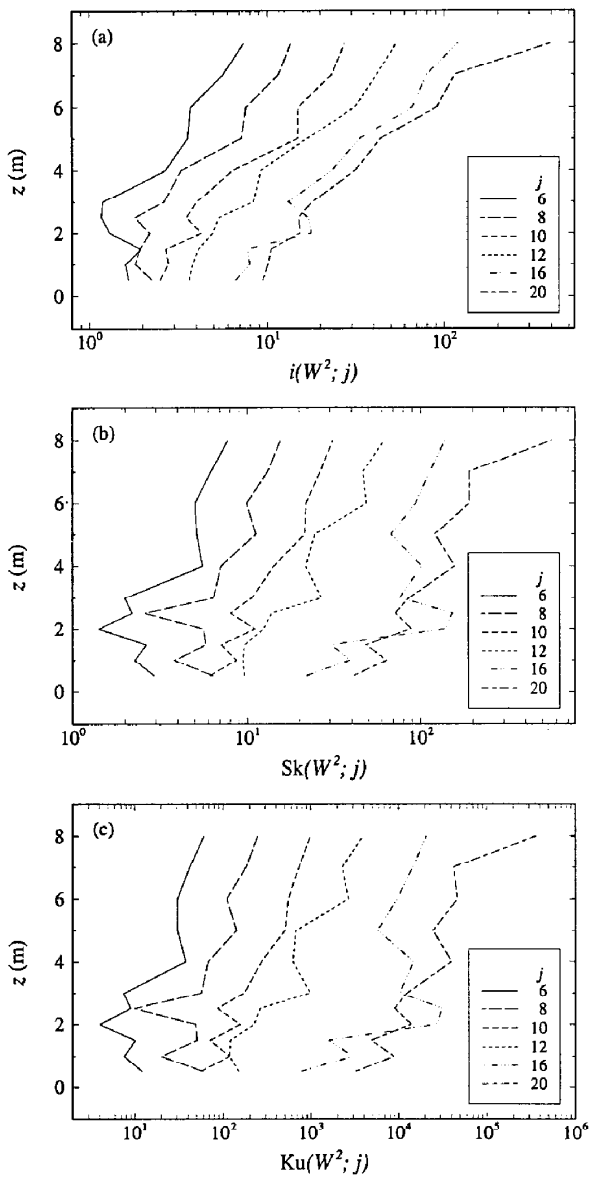

Fig. 7. Vertical profiles of wavelet statistics of the squared discrete detailed signal $W^2_{j,k}$: (a) fluctuation intensity, $i(W^2; j)$; (b) skewness, $\mathrm{Sk}(W^2; j)$; and, (c) kurtosis, $\mathrm{Ku}(W^2; j)$ for $j = 6$, 8, 10, 12, 16, and 20. The data were taken from Trial CC24.

Figure 8 illustrates the correlation between consecutive octave scales for the second-order wavelet coefficients (wavelet energy), $R_j^{(2)}$ (cf. Equation (9)). This information reflects the temporal correlation of the concentration variance (energy) between adjacent scales j and $j + 1$. At a given height, the correlation increases

with increasing frequency (increasing j, or decreasing scale). The strong correlation between scales suggests the presence of a concentration variance cascade process in which in-plume mixing of clean air with plume material transfers fluctuation variance from the larger scales to the smaller scales. Furthermore, at a fixed scale, the correlation is seen to increase generally with increasing height from the ground. In particular, the correlation rises steadily in the scales corresponding to the inertial-convective subrange. Hence, the more thorough mixing of plume material by the intense small-scale turbulence near the ground leads to a reduction in the interscale correlation between concentration variance events.

4.3. Probability Density Function of Wavelet Coefficients

It is apparent from Figure 2 that the mean and variance of $W_{j,k}$ contain little information about the detailed signal. In consequence, we consider the pdf of the discrete detailed signal $W_{j,k}$ normalized in root-mean-square (rms) units (viz., the pdf of $\alpha_{j,k} \equiv W_{j,k}/\sigma(W; j)$) at a fixed scale index j. This pdf was estimated by the kernel method (Silverman, 1982). The kernel estimate of the pdf at the point α, given the rms normalized detailed signal $\alpha_{j,k}$ at a fixed scale index j, has the following form:

$$P(\alpha) = \frac{1}{nh} \sum_{k=0}^{2^j-1} K\left(\frac{\alpha - \alpha_{j,k}}{h}\right),$$

where $n \equiv 2^j$ is the number of detailed signal samples at scale j, K is the kernel function, and h is the width of the kernel function. The pdfs were estimated with the standard Gaussian kernel function (i.e., $K(x) = \exp(-x^2/2)/\sqrt{2\pi}$) with h chosen in accordance to the maximal smoothing principle as described by Terrell (1990). The number of samples n decreases with the scale index j, and it was judged that the pdf of $\alpha_{j,k}$ cannot be accurately estimated for $j \lesssim 10$.

Figure 9 shows the semi-logarithmic plots of pdfs of $\alpha_{j,k}$ for scales from $j =$ 10 to 20 (corresponding to periods from 2.048 to 0.002 s). The standard Gaussian pdf has been included in the plots for comparison. The data were taken from Trial CC05 for the sampling height at 1.5 m (cf. Figure 2). The pdfs are nearly Gaussian at the larger scales, but the tails of the pdfs grow progressively longer at the smaller scales (viz., the tails are more strongly spread when compared with a Gaussian pdf). The long tails of the pdfs arise from rare, large-amplitude fluctuations interspersed among the periods of small turbulent activity, and the latter characteristics are evident at the smaller scales on examination of the discrete detailed signals exhibited in Figure 2. The long tails of the pdfs at small scales are consistent with the increasing intermittency and wavelet coefficient kurtosis (cf. Figure 3) of the detailed signal at these scales. Finally, the pdfs of the wavelet coefficients are roughly symmetric, although there is a small departure from perfect symmetry, as demonstrated by the wavelet coefficient skewness (not shown) which

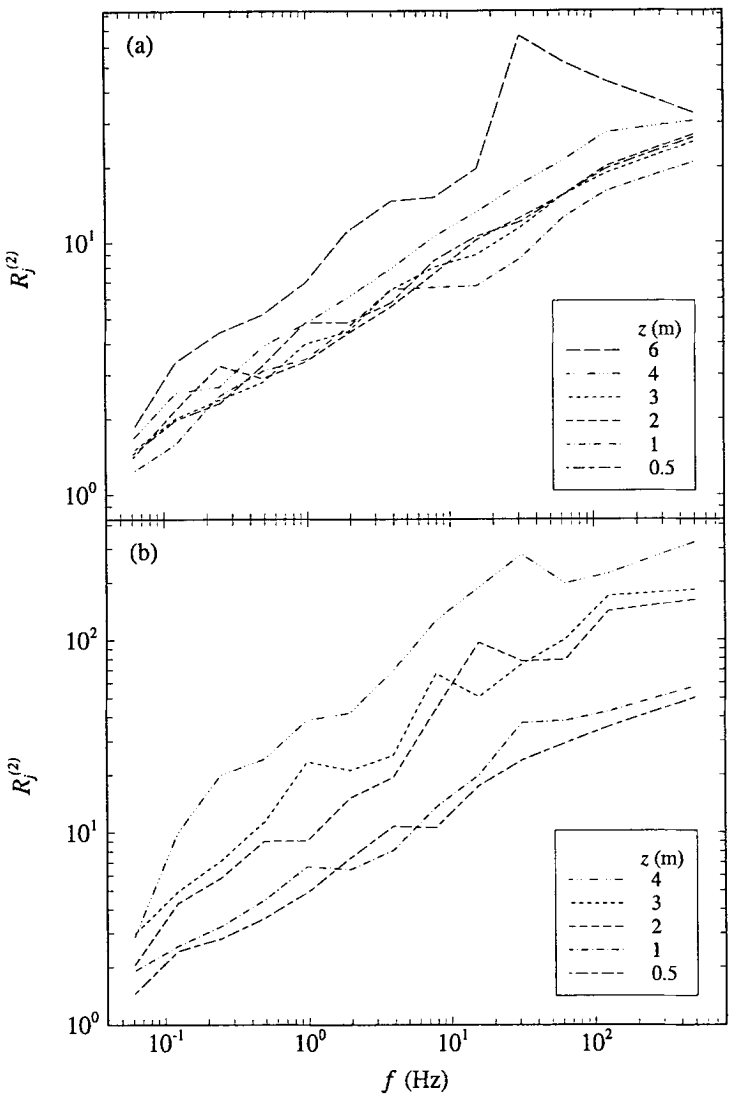

Fig. 8. The correlation, $R_j^{(2)}$, of the second-order wavelet coefficients between scales j and $j+1$ (equivalently, frequencies f_j and f_{j+1}) for (a) Trial CC05 and (b) Trial CC24 at a number of heights z above the ground. The frequency f corresponding to scale index j is defined as $f = f_j \equiv 2^j T^{-1}$, where T is the sampling time.

typically gave absolute values between about 0.1 and 1 with higher values to the large-scale side (i.e., small j), and lower values around zero at the smallest scales.

Figure 10 illustrates the change in the pdf shape of $\alpha_{j,k}$ for a fixed scale index $j = 20$, at a number of heights above the ground. The data for this example are taken from Trial CC05. At a fixed scale, the pdf tails are more elongated higher up in the plume. In particular, the fine-scale plume structure near the ground appears

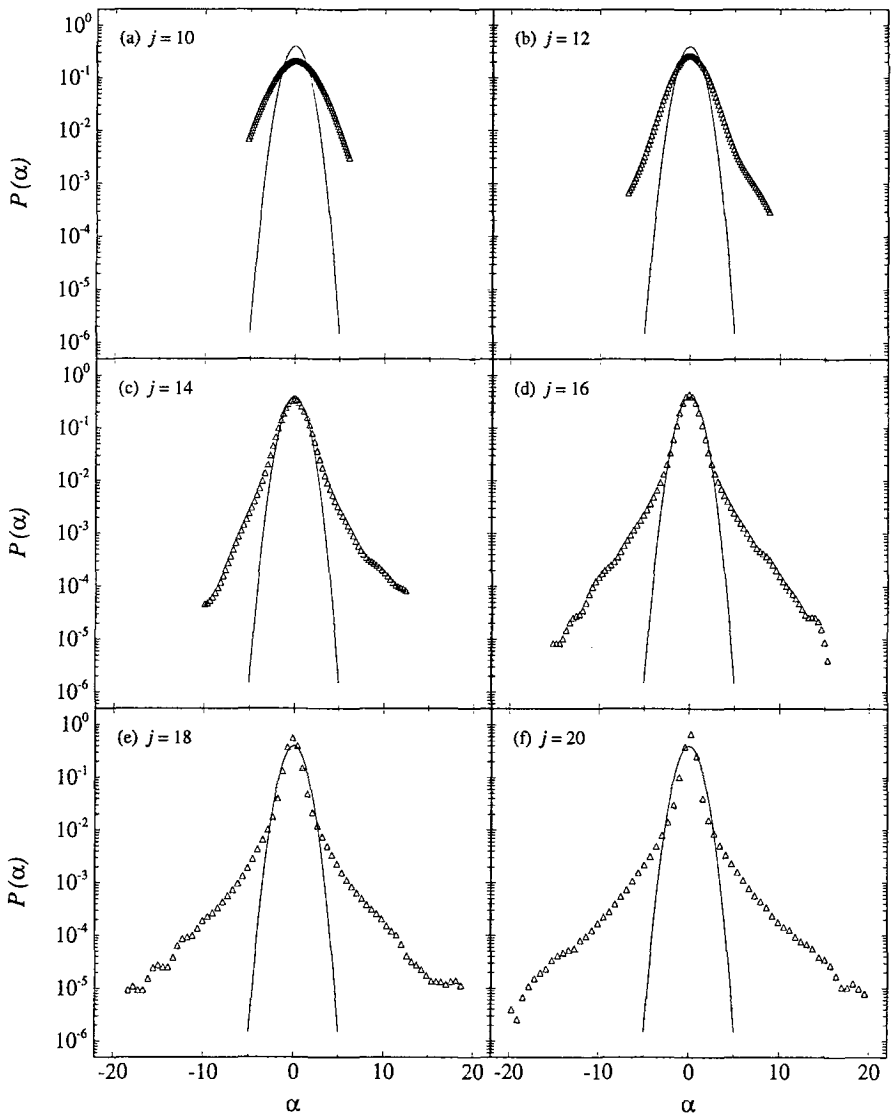

Fig. 9. Semi-logarithmic plots of the pdfs, $P(\alpha)$, for the normalized discrete detailed signal (wavelet coefficients) $\alpha \equiv W_{j,k}/\sigma(W; j)$ for six different scales ranging from $j = 10$ to 20. The pdfs are compared with a standard Gaussian pdf shown by the solid curve in each plot. The data were taken from the concentration time series shown in Figure 2.

to be more smoothed out, leading to pdfs of $\alpha_{j,k}$ with noticeably shorter tails. Hence, the change in the pdf shapes with z at a fixed scale is consistent with a more intermittent structure of concentration fluctuations higher up in the plume.

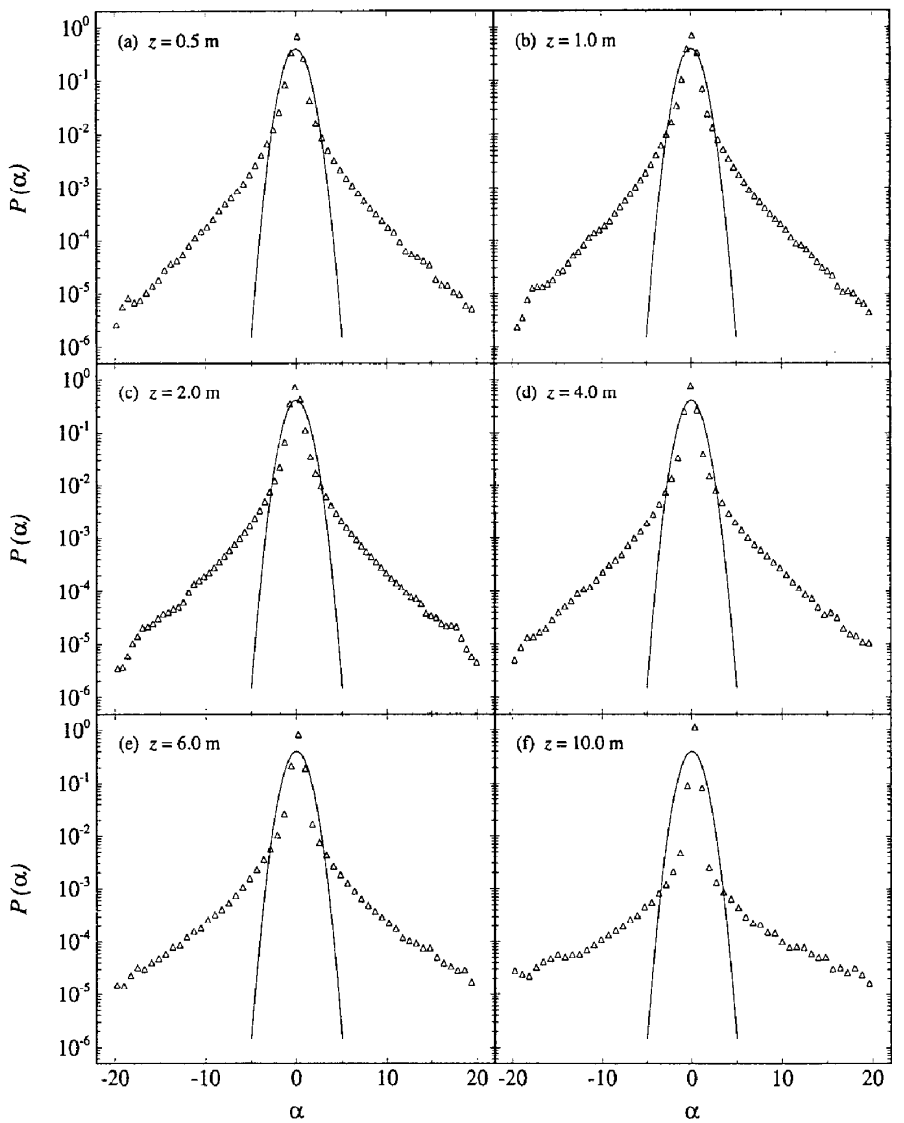

Fig. 10. Semi-logarithmic plots of the pdfs, $P(\alpha)$, for the normalized discrete detailed signal (wavelet coefficients) $\alpha \equiv W_{j,k}/\sigma(W; j)$ for six different heights above the ground at a fixed scale index $j = 20$. The pdfs are compared with a standard Gaussian pdf shown by the solid curve in each plot. The data were taken from the Trial CC05.

We now explore quantitatively the tail behaviour of the detailed signal pdfs with scale at a fixed height, and with height at a fixed scale. Towards this objective, we fit the pdf tails with a stretched-Gaussian pdf with the form

$$P(\alpha) = P(0)\exp(-\lambda|\alpha|^q), \tag{10a}$$

where the values of $P(0)$ and λ are determined by the constraints $\int_{-\infty}^{\infty} P(\alpha)d\alpha = 1$ and $\langle \alpha^2 \rangle = 1$, so

$$P(0) = \frac{q}{2\Gamma(1/q)[\Gamma(1/q)\Gamma(3/q)]^{1/2}}, \tag{10b}$$

and

$$\lambda = \left[\frac{\Gamma(3/q)}{\Gamma(1/q)}\right]^{q/2}. \tag{10c}$$

Here, $\Gamma(x)$ is the gamma function and q is a "stretching" exponent that characterizes the tail slope of the pdf. We interpret q as a measure of the degree of intermittency of the underlying signal (viz., the smaller the value of q, the longer the pdf tail, and the more intermittent the underlying signal). Note here that the term intermittency should be taken to indicate an elongated tail in the pdf for concentration variations at a given scale, rather than the fraction of non-zero concentration against zero concentration as sometimes defined. We refer to the stretched-Gaussian form of Equation (10) as the generalized q-Gaussian (gqG) pdf. Clearly, the gqG pdf reduces to the standard Gaussian and Laplacian (two-sided exponential) pdfs when $q = 2$ and 1, respectively.

The intermittency exponent, q, was determined by plotting $\ln(\ln(P(0)/P(\alpha)))$ versus $\ln(|\alpha|)$. If the pdf tails of $\alpha \equiv \alpha_{j,k}$ are well represented by the gqG pdf, then a straight line with slope q will be obtained. A typical example of such a plot is shown in Figure 11 for data taken from Trial CC05 at a detector height of 1 m for the detailed signal at scale index $j = 17$ (0.016 s period). The example shown here corresponds to the left-side or negative tail of the pdf (i.e., $\alpha < 0$). On this plot, it is readily seen that the pdf consists of two parts (regions), each of which is associated with a particular linear regime. The central region of the pdf, corresponding to values of α around zero, consists of an extruded peak. This pointed central region of the pdf corresponds to Region I shown in Figure 11. This region is restricted roughly to $|\alpha| \lesssim 2.7$ (cf. Figure 9) or, equivalently, to the region $\ln(|\alpha|) \lesssim 1$ (cf. Figure 11). The tail region of the pdf is associated with Region II shown in Figure 11. The transition between Regions I and II occurs at $|\alpha| \approx 2.7$, and corresponds to a break in the pdf shape from the pointed central region to the more elongated tail region. A very good straight-line fit can be obtained in the tail region, as shown in the inset of Figure 11. Typically, the coefficient of determination for the least-squares fit is greater than about 0.995. A least-squares fit to Region II then yields the tail slope or intermittency exponent, q (cf. inset of Figure 11). It is noted that the organization of small-scale intermittency in plume concentrations is different from the hyperbolic intermittency (i.e., $P(\alpha) \sim \alpha^{-q}$ for large α) obtained by Lovejoy and Schertzer (1985) for atmospheric dynamics.

Figure 12 shows the intermittency exponents (tail slopes) q plotted versus time scale or period τ for a fixed height z in the plume. The data have been taken

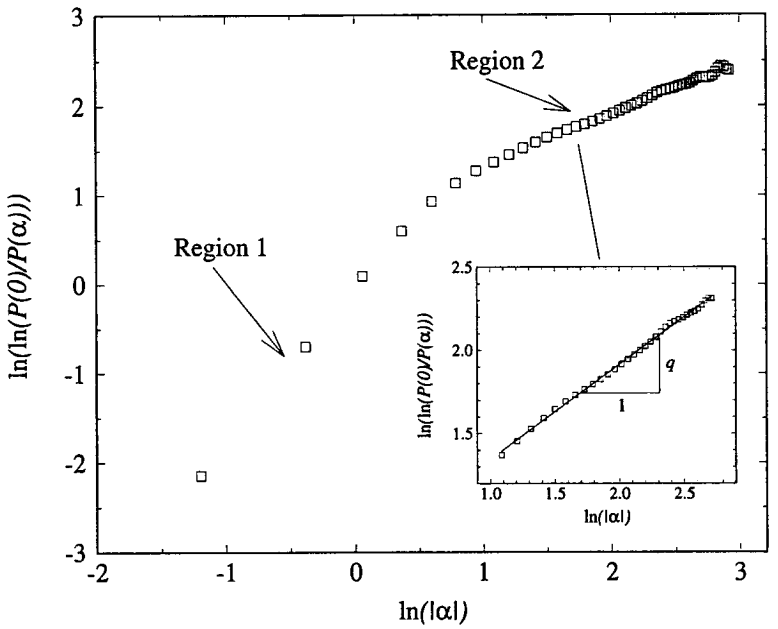

Fig. 11. A typical plot of $\ln(\ln(P(0)/P(\alpha)))$ versus $\ln(|\alpha|)$ for data taken from Trial CC05 at a detector height of 1 m. The plot was constructed from the negative tail ($\alpha < 0$) of the detailed signal pdf at the fixed scale index $j = 17$. The tail slope or intermittency exponent q is obtained by determining the slope of the linear least-squares fit to the points in Region II corresponding to $\ln(|\alpha|) \geq 1$ (inset).

from Trial CC05 for $z = 2$ m (Figure 12(a)), and Trial CC24 for $z = 1.5$ m (Figure 12(b)). The tail slopes from both sides of $P(\alpha)$ are shown in Figure 12. Generally, the asymmetry in the positive and negative tails of the pdfs is small. Hence, we ignore the small differences between the positive and negative tails, and report the tail slope q as the average of these two estimates. When plotted on a double logarithmic plot as in Figure 12, it is seen that $q(\tau)$ can be fitted roughly by 2 straight lines. At the intermediate time scales associated with the inertial-convective subrange, the dependence of q on τ can be described by a power-law of the form $q(\tau) \sim \tau^a$ ($a > 0$). The value of the power-law exponent a appears to vary with downwind distance, plume height, and stability stratification, but typically was found to lie in the range from about 0.25 to 0.35 for the datasets we examined. For $\tau \lesssim \tau_1$ (cf. Figure 12), q is approximately constant, and the effects of molecular diffusion begin to become important. The large-gradient regions that are generated at these small scales are also the regions most strongly affected by molecular diffusion. This preferential smoothing leads to the near constancy of q with scale here. We found that the time scale τ_1 is comparable to the Taylor micro-time scale, $T_T \equiv [2\sigma_\chi^2/\overline{(\partial\chi/\partial t)^2}]^{1/2}$ (indicated by the arrows in Figure 12). Hence, τ_1 or T_T can be interpreted as the time scale below which dissipation *begins* to

become important and, as such, marks the small-scale end of the inertial-convective subrange and the large-scale beginning of the near-dissipation subrange. Finally, the fact that q is not a constant in the inertial-convective subrange implies that the pdf of concentration increments over this range of scales is not self-similar, and provides evidence for (but does not prove) the multifractal scaling nature of plume concentrations in the inertial-convective subrange. Indeed, Vainshtein *et al.* (1994) demonstrated that tails of the pdf with the stretched-Gaussian form exhibited in Equation (10a) can be associated with a monofractal scaling behaviour only if q is a constant that does not depend on scale.

Figure 13 shows the vertical dependence of the tail slope q at a fixed scale (j = 18, or 0.008 s period) for Trials CC05 and CC24. The tail slopes shown in Figure 13 represent the average from the negative and positive pdf tails. The higher up in the plume, the more extended the tails of the pdf appear to be. This effect is most likely due to the increased intermittency higher up in the plume (viz., the fluctuations near the surface are subject to more vigorous small-scale mixing which tends to homogenize the plume internally by mixing small plume elements together). The data in Figure 13 suggest that q decreases approximately linearly with increasing height z above the surface. This is indicated by the solid lines in Figure 13 which show the linear least-squares fit of q to z.

4.4. Phase coherency and concentration variance cascade

Eddies (scales) smaller than the instantaneous plume width result in internal mixing of the contaminant and entrained clean air. This process transfers concentration variance (energy) from large scales to small scales producing the inertial-convective subrange behaviour observed in the concentration spectrum. The fluctuation variance transfer between scales produces an extremely complex and intermittent structure of contaminant elements on scales smaller than the instantaneous plume width. The variance cascade process that generates the small-scale in-plume intermittency must impose a definite phase coherency between the many different-sized eddies that participate in this process.

In order to demonstrate the relationship between phase coherency and the cascade process, we Fourier transformed the concentration time series shown in Figure 2, randomized the phase uniformly in $[0, 2\pi)$ while preserving the amplitude, and inverse Fourier transformed the result to produce a phase-randomized concentration signal. Because the Fourier concentration amplitude is unchanged, the concentration Fourier power spectra for the original and phase-randomized concentration signal are identical. Furthermore, the Haar concentration spectra of the two signals are virtually identical (not shown), each exhibiting the characteristic $-5/3$ slope of the inertial-convective subrange.

Despite the presence of the $-5/3$ slope in the spectrum, the phase-randomized signal does not appear to exhibit the properties characteristic of a variance cascade process in physical space. Figures 14(a) and (b) display the wavelet coefficient

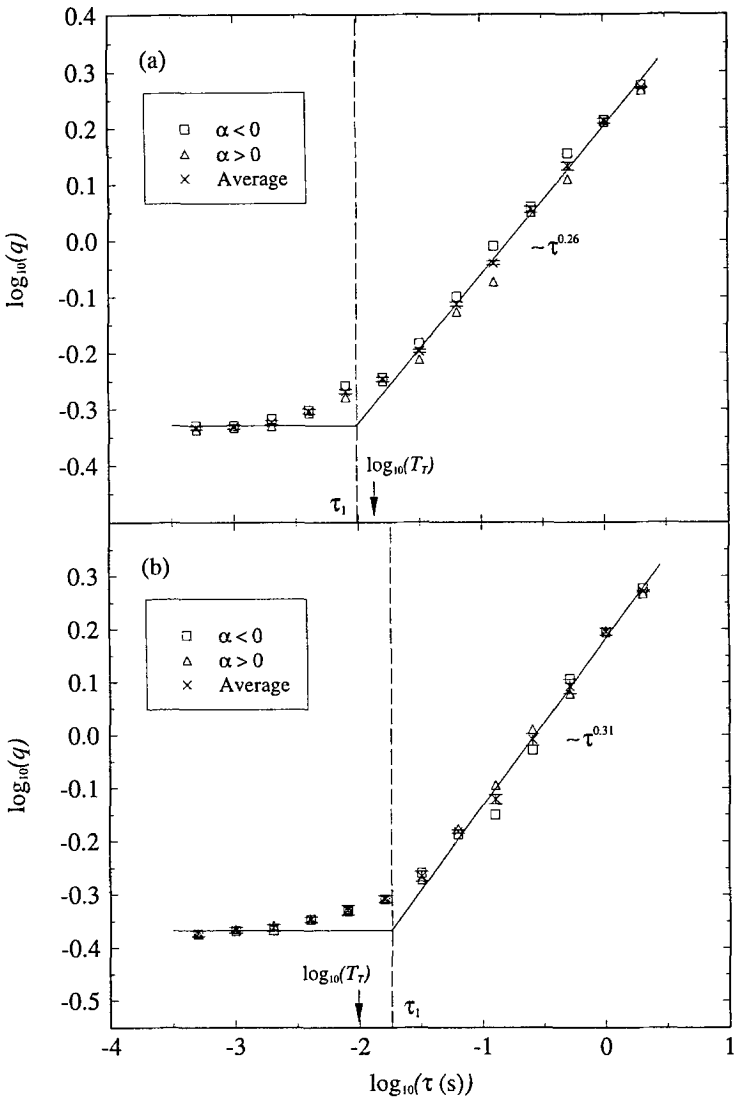

Fig. 12. The dependence of the intermittency exponenent, q, on time scale, τ (or, equivalently, on the scale index j) for concentration data obtained from (a) Trial CC05 at detector height $z = 2$ m and (b) Trial CC24 at detector height $z = 1.5$ m. The intermittency exponents obtained from the negative ($\alpha < 0$) and positive ($\alpha > 0$) tails of $P(\alpha)$ are shown, as well as the values of q obtained by taking the average of the estimates from the negative and positive pdf tails. The error bars shown for the latter values of q have been estimated from the standard errors in q obtained from the linear regression of $\ln(\ln(P(0)/P(\alpha)))$ on $\ln(|\alpha|)$ (cf. Figure 11). The time scale τ_1 below which q remains approximately constant with decreasing scale is indicated by the dashed vertical line. Arrows mark the corresponding Taylor micro-time scales, T_T.

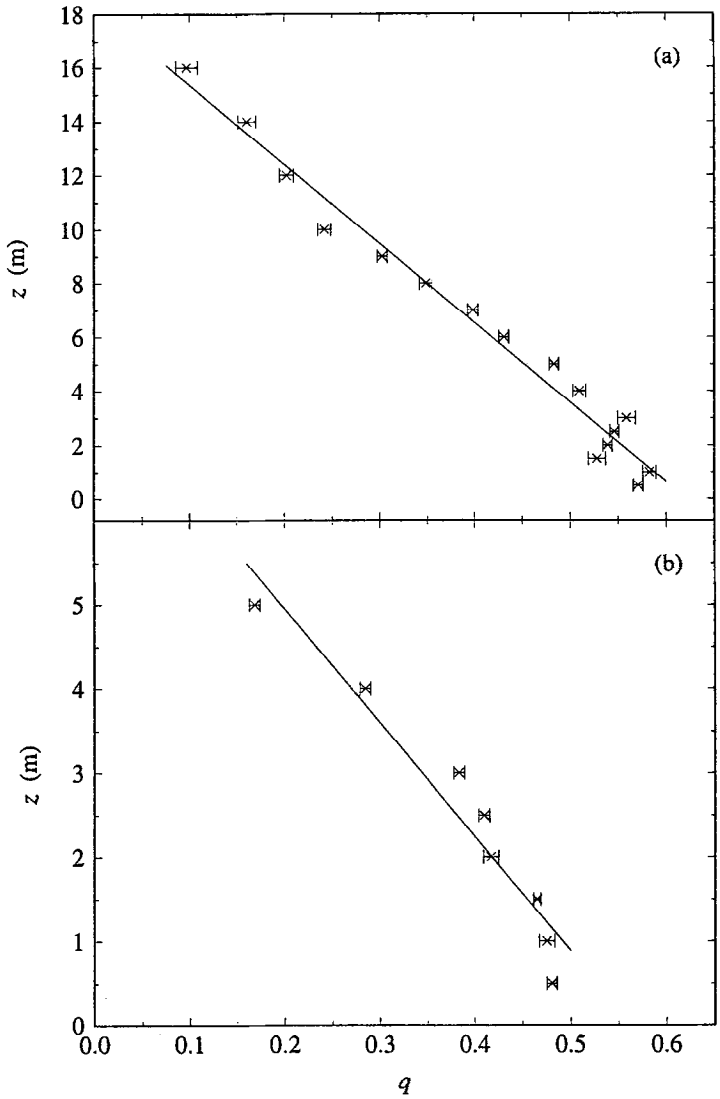

Fig. 13. The dependence of the intermittency exponent, q, on height, z, at the fixed scale index j = 18 (0.008 s period or dilation) for (a) Trial CC05 and (b) Trial CC24. The straight lines correspond to the linear least-squares fits of q to z. The error bars shown represent the estimated standard errors in q obtained from the linear regression of $\ln(\ln(P(0)/P(\alpha)))$ on $\ln(|\alpha|)$ (cf. Figure 11).

kurtosis and the correlation of the second-order wavelet coefficients at consecutive scales, respectively, for the original and phase-randomized concentration signals. Unlike the original signal whose wavelet coefficient kurtosis increases with decreasing scale (increasing frequency f or scale index j), the wavelet kurtosis of the phase-randomized signal remains nearly constant at about 3 for all scales. This implies that the pdf of the wavelet coefficients is approximately Gaussian at

all scales for the phase-randomized signal; hence, the increasing spatiotemporal intermittency at decreasing scales that is characteristic of the original concentration signal is destroyed completely by the phase randomization. The latter is confirmed in the wavelet coefficient pdfs of the phase-randomized signal shown in Figure 15. Note that these pdfs show close to Gaussian behaviour at all scales, in sharp contrast to the strongly non-Gaussian behaviour of the corresponding pdfs for the original signal (cf. Figure 9 where the pdfs are seen to exhibit very distinctive extended exponential tails at the small scales). Moreover, the strong correlation between wavelet coefficients of different scales within the inertial-convective subrange of the original signal is completely absent in the phase-randomized signal (cf. Figure 14(b)). In summary, it appears that the intermittent concentration structures created by the nonlinear straining of the turbulent velocity field and leading to the concentration variance cascade in the inertial-convective subrange requires (or generates) a phase coherency in the concentration signal. In other words, a random phase is not consistent with the concentration variance cascade process.

5. Epilogue: Unified Picture of Plume Dispersion and Contaminant Texture

In this study, we applied a scale-conditioned data analysis method based on the orthonormal wavelet representation to some very high-resolution plume concentration data. This representation can be interpreted as the decomposition of the signal into a set of independent frequency channels in scale space (wavenumber space) while preserving the structure of the signal in physical space. In consequence, the wavelet decomposition can provide insights into the concentration fluctuation phenomenon that would not have been possible otherwise by more conventional methods (e.g., those based on extracting global concentration statistics such as mean concentration, concentration variance, etc.).

The results of the wavelet decomposition of the fluctuating concentration described in Sections 4.1 to 4.4 can be combined together to give a very detailed picture of plume concentration structure and texture. The concentration fluctuations observed in a dispersing plume are the result of turbulent motions on a wide range of scales that reflect the simultaneous effects of many different-sized eddies. At a fixed distance (travel time) from the source, turbulent eddies that are large compared to the instantaneous plume width result in bulk meandering of the plume (external fluctuations). The latter scales will waft around the entire plume, but not result in any nonlinear cascade of the concentration variance onto smaller scales.

Scales comparable to or smaller than the instantaneous plume width will break up the plume to initiate a turbulent cascade of concentration variance from the larger-scale motions onto the smaller-scale motions. This intermediate range of scales with negligible dissipation corresponds to the stirring process inside the instantaneous plume boundaries which produce the internal fine-scale fluctuations. These scales correspond to the inertial-convective subrange of plume dispersion

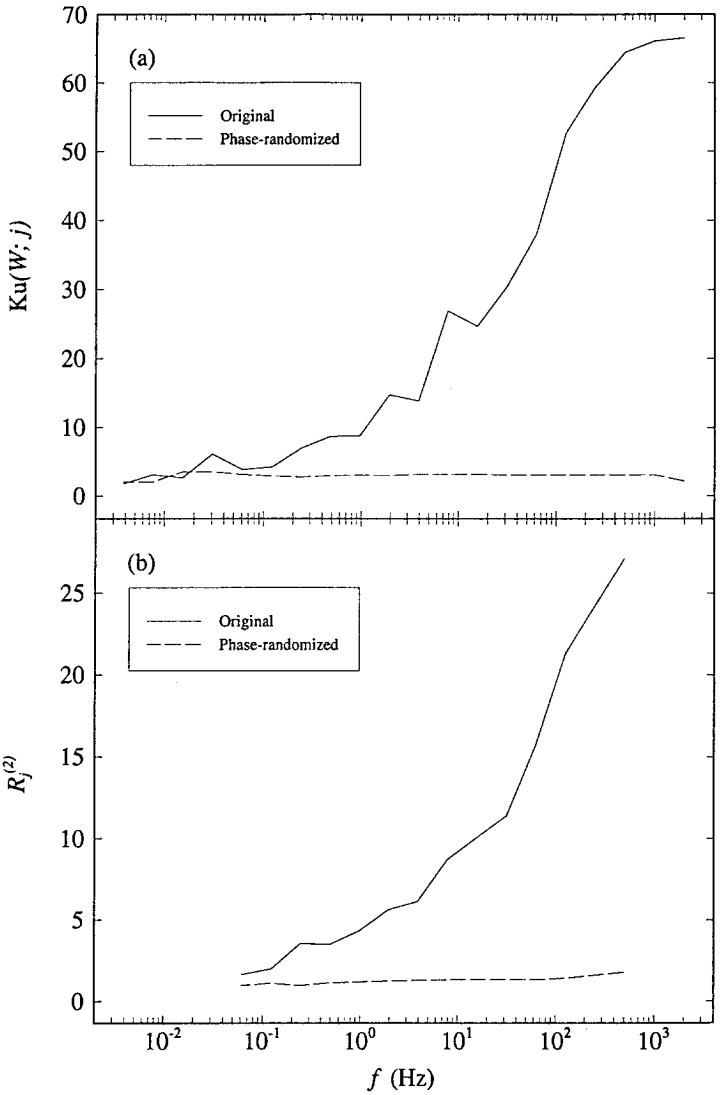

Fig. 14. A comparison of the behaviour of (a) the wavelet coefficient kurtosis, Ku(W; j), and (b) the correlation of the second-order wavelet coefficient between consecutive scales, $R_j^{(2)}$, for an observed fluctuating concentration signal and a phase-randomized concentration signal. The data for this example were taken from Trial CC05 for the detector at z = 1.5 m (cf. Figure 2).

with its characteristic $-5/3$ scaling law (cf. Figure 4 where the $-5/3$ scaling law in the concentration spectrum was found to be robust with respect to the choice of a basis set). Within the inertial-convective range of motions, turbulent eddies with scales in the large end of the range (i.e., scales comparable to the instantaneous plume width σ_i) cause progressive distortion of the plume boundary as packets of clean air are entrained into the body of the plume. On the other hand, scales

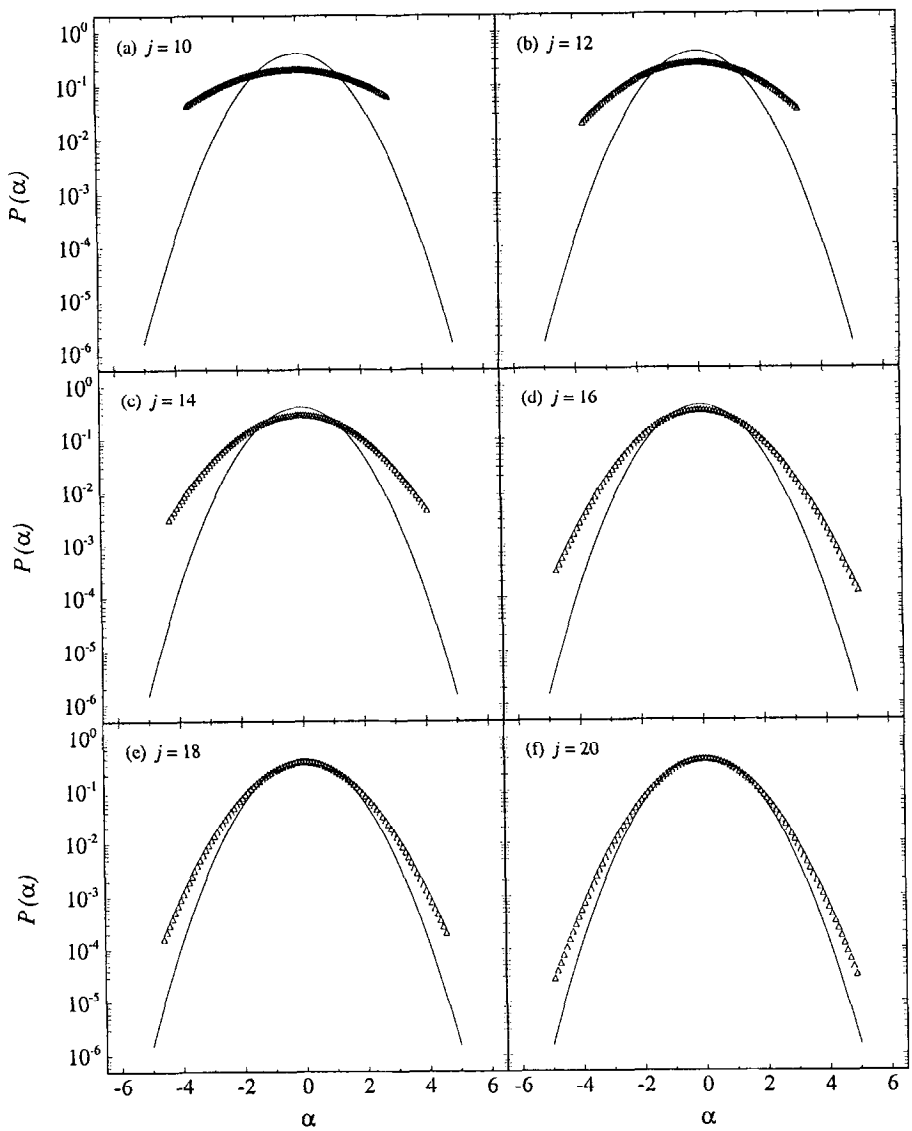

Fig. 15. Fig. 15. Semi-logarithmic plots of the pdfs, $P(\alpha)$, for the phase-randomized discrete detailed signal (wavelet coefficients) $\alpha \equiv W_{j,k}/\sigma(W; j)$ for six different scales ranging from $j = 10$ to 20. The pdfs are compared with a standard Gaussian pdf shown by the solid curve in each plot. The original data used in the phase-randomization were taken from the concentration time series shown in Figure 2.

in the smaller end of the range (i.e., scales smaller than σ_i) result in mixing of the contaminant and entrained clean air, producing complicated non-Gaussian instantaneous distributions of in-plume concentration.

Although the $-5/3$ scaling law remains constant throughout the entire inertial-convective subrange of scales, we found that the degree of intermittency and

non-Gaussianity of the eddies varies considerably within this range (cf. Figures 3, 5, and 9). The latter observation is important for determination of the nature of contaminant texture (i.e., organization of fine-scale structure) in dispersing plumes. In particular, we found that eddies corresponding to the larger scales of the inertial-convective subrange were more space-filling in physical space (cf. Figure 2), and that the fluctuating concentration at these scales was approximately Gaussian (cf. Figures 3 and 9). The space-fillingness and Gaussian behaviour of these "eddies" (scales) is manifested in the high degree of phase decorrelation (randomness) between consecutive octave scales measured at the larger inertial-convective scales (cf. Figure 14). The latter behaviour is observed also in a phase-randomized concentration signal (cf. Figures 14 and 15), and may be intimately related to the "global" nature of the in-plume concentration structure signal at the larger inertial-convective scales. More importantly, our detailed analysis demonstrated the increasing intermittency (or decreasing space-fillingness of eddies) and non-Gaussianity of the fluctuating concentration (cf. Figure 9) over progressively smaller scales in the inertial-convective subrange. The latter behaviour appears to be intimately connected with some form of phase organization (i.e., coherency or non-randomness of phase) between consecutive octave scales at the smaller inertial-convective scales (cf. Figure 14). We associate the latter behaviour with the presence of localized coherent plume concentration structures (eddies) at the smaller inertial-convective scales.

The distribution of concentration variance (energy) and phase in the inertial-convective scales as revealed by the wavelet decomposition suggests the following conceptual model of in-plume concentration structure in physical space. The smaller inertial-convective scales appear to be associated with some small-scale coherent (phase-correlated) and non-Gaussian concentration structures that are highly intermittent in space. These localized structures are evolving and interacting with the surrounding Gaussian (approximately) and diffuse (phase-scrambled) background concentration component that is space-filling; and, the latter "global" component of the in-plume concentration structure appears to be associated with the larger inertial-convective range scales. In summary, the picture of the in-plume concentration structure that emerges is as follows: there are local coherent small-scale concentration structures that are evolving in a global diffuse background concentration component. This picture of concentration structure in a dispersing plume is consistent with the structure of homogeneous scalar fields developed by Batchelor (1952), Batchelor (1959), Batchelor *et al.* (1959), and Townsend (1959). Along the same lines, a two-state physical model for the concentration probability density function based on the "picture" of strands or sheets of high concentration embedded in a low concentration background (and, predicated on the separation of the time scales of the short-term turbulent convective motions and the long-term molecular diffusion) has been proposed by Chatwin and Sullivan (1990).

This picture of the two component in-plume concentration structure is most likely the direct consequence of the simultaneous effects of turbulent stirring (i.e.,

strain-induced stretching of the inter-material surface) and molecular mixing (i.e., molecular diffusion of contaminant across the inter-material surface). It is this two-stage process (viz., stretching and convolution of inter-material surfaces by the turbulence followed by molecular mixing across a thin layer) that ultimately determines the contaminant texture in a dispersing plume. Indeed, for scales representative of the inertial-convective subrange, contaminant blobs are simultaneously distended, folded, and distorted by the turbulent convective motions into ever thinning and convoluted strands or ribbons. This causes the area of a concentration isopleth to grow roughly exponentially in time, resulting in greatly enhanced gradients arising from the interleaving of material surfaces. It is plausible but not obvious to associate the stretching and folding effect with the turbulent cascade of fluctuation variance down the scales of the inertial-convective subrange, but it must be emphasized that the latter process is quite unlike the usual Kolmogorov-type cascade picture involving an eddy breakdown or fragmentation process. In the present scenario, we associate the ever thinning strands of contaminant material (e.g., small-scale filamentary structures) arising from the compressive straining motions with the local small-scale coherent (phase-correlated) concentration structures deduced from the wavelet decomposition. The latter connection would follow if we regard the contaminant strands as wavepackets consisting of a large number of flow modes with wavelengths less than the mean diameter of the strand. Mechanically, the turbulent convective stirring can increase the concentration gradients until the thinning of the contaminant strands is balanced by the thickening due to molecular diffusion, which acts most effectively at the smallest scales of the flow. Mixing by molecular diffusion *begins* to become important at the Taylor microscale, which marks small-scale end of the inertial-convective subrange, and beginning of the near-dissipation subrange (cf. Figure 12). Note the Taylor microscale is not the characteristic size of the dissipative eddies themselves, which would be determined by the much smaller Batchelor scale (the latter would be similar to the Kolmogorov scale at which viscous effects in the velocity field become important, as the Schmidt number ($\equiv \nu/D$, where ν is kinematic viscosity and D is molecular diffusivity) is about 1 for the diffusion of propylene in air).

When the ever thinning strands of contaminant material permeate the instantaneous plume boundaries to the extent that their mean separation is less than the distance over which molecular diffusion is effective (e.g., the Batchelor diffusive cut-off length), neighbouring strands will begin to merge to form groups of merged filaments. The merging process destroys the phase organization in the individual contaminant strands (or, more precisely, the phase-coupling of local regions of high-wavenumber Fourier space that we associate with the ever thinning strands of contaminant in physical space). Eventually, the merged strands will approach a length scale comparable to the instantaneous plume width, and the concentration of the merged groups would, at this stage of evolution, become uniformly mixed to form the diffuse (phase-scrambled) background concentration component described earlier. Also, the relaxation of regions of intense gradient by

molecular diffusion, and the merging of these regions to form the low background concentration would be expected to generate a Gaussian distribution. Hence, the simultaneous action of turbulent stirring and molecular diffusion appears to produce a plume texture that is consistent with that deduced from a wavelet decomposition of the fluctuating concentration; namely, the in-plume concentrations are composed to two components (viz., a high concentration component localized in thin filaments of material (e.g., the localized, coherent, small-scale concentration structures) surrounded by an approximately Gaussian background concentration "sea" made up of independent strands that have merged again due to molecular diffusion to form a low concentration component of contaminant material fully molecularly diffused into the entrained ambient air). Finally, the thickness and density of a contaminant strand that "floats" in the Gaussian background concentration "sea" must reflect the rate-of-strain history encountered by the contaminant element because the history of the concentration gradient in the element can depend only on the straining experienced by that element along its Lagrangian trajectory.

This work also demonstrated that increased mean wind shear (such as that which exists near the ground) can alter the contaminant texture in a dispersing plume through the action of continued stretching of plume material. In this case, the mean shear or large-scale strain can act on scales larger than the instantaneous plume width to distend blobs of contaminant into elongated structures over most of the volume occupied by the instantaneous plume. Here, it is plausible that the small-scale mixing (e.g., the process that counteracts the growth of the intermaterial surface) in the plume is controlled by the large-scale strain rate (e.g., the mean wind shear) since the small-scale velocity modes (e.g., stretching of vortex tubes), responsible for the enhanced diffusivity of the scalar, are present only because of the large-scale strain acting on them.

What is the correspondence between the effects of the mean wind shear on the concentration structure in the physical space and on the scale-conditioned wavelet coefficient statistics? The net effect of the increased mean wind shear near the ground is to smooth the concentration structure in the plume, leading to less intermittent distributions of concentration structure at all scales in the inertial-convective subrange compared with those measured higher up in the plume (cf. Figures 6, 7, 10, and 13). This large-scale strain-induced mixing along the Lagrangian trajectory of contaminant elements (e.g., scalar-marked fluid elements) moving through regions of enhanced mean shear (e.g., near the ground) is expected to decrease the mixing time of the elements. The influence of the large-scale strain on the mixing time of contaminant elements is reflected in the tails of wavelet coefficient pdfs (cf. Figures 10 and 13) that embody information on the distribution of concentration increments over a given length scale. Indeed, the latter quantities must simply reflect the particular strain histories of the contaminant elements; and, contaminant elements that have been highly strained (such as near the ground) thereby decay more rapidly, leading to shorter tails in the wavelet coefficient pdfs.

The strain-enhanced mixing near the ground can be pictured as follows. The increased mean shear causes the area of the intermaterial surface to grow at a greater rate (since the surface area growth rate is proportional to the root-mean-square of the strain), and the latter accelerated growth can greatly facilitate the merging of neighbouring contaminant strands (ribbons) to form groups of merged streaks in which the concentration is fully mixed (viz., regions that have been highly strained typically experience stronger diffusion than other regions). This accelerated merging of strands is consistent with the reduction of the interscale correlation between concentration variance events in regions of the plume subjected to increased mean shear (cf. Figure 8). The latter effect is expected because phase correlation is intimately linked to intermittency and the presence of small-scale coherent concentration structures. The merging of these small-scale structures reduces the phase organization, producing a stronger diffuse background concentration; and, the latter is consistent with a contaminant texture that is observed to be more thoroughly mixed in the presence of an increased mean wind shear. What cannot be inferred from the present analysis is the dynamical role that is played by vortical structures (e.g., vortex tubes and sheets) in the turbulent diffusion and mixing of plume elements near the ground (e.g., in regions of increased large-scale strain). There is clearly a need for further experimentation in this area, requiring as such simultaneous and highly resolved spatial and temporal measurements of the plume concentration, velocity, and vorticity fluctuations near the ground.

Argoul, F., Arneodo, A., Grasseau, G., Gagne, Y., Hopfinger, E. J., and Frisch, U.: 1989, 'Wavelet Analysis of Turbulence Reveals the Multifractal Nature of the Richardson Cascade', *Nature* **338**, 51–53.

Bara, B. M., Wilson, D. J., and Zelt, B. W.: 1992, 'Concentration Fluctuation Profiles from a Water Channel Simulation of a Ground-Level Release', *Atmos. Environ.* **26A**, 1053–1062.

Batchelor, G. K.: 1959, 'Small-scale Variation of Convected Quantities Like Temperature in Turbulent Fluid. Part 1. General Discussion and the Case of Small Conductivity', *J. Fluid Mech.* **5**, 113–133.

Batchelor, G. K.: 1952, 'The Effect of Homogeneous Turbulence on Material Lines and Surfaces', *Proc. Roy. Soc. Lond. A* **213**, 349–366.

Batchelor, G. K., Howells, I. D., and Townsend, A. A.: 1959, 'Small-scale Variation of Convected Quantities Like Temperature in Turbulent Fluid. Part 2. The Case of Large Conductivity', *J. Fluid Mech.* **5**, 134–139.

Chatwin, P. C. and Sullivan, P. J.: 1990, 'A Simple and Unifying Physical Interpretation of Scalar Fluctuation Measurements from Many Turbulent Shear Flows', *J. Fluid Mech.* **212**, 533–556.

Chui, C. K.: 1992, *An Introduction to Wavelets*, Academic Press, San Diego, 264 pp.

Collineau, S. and Brunet, Y.: 1993, 'Detection of Turbulent Coherent Motions in a Forest Canopy. Part I: Wavelet Analysis', *Boundary-Layer Meteorol.* **65**, 357–380.

Daubechies, I.: 1992, *Ten Lectures on Wavelets*, Society for Industrial and Applied Mathematics, Philadelphia, 357 pp.

Daubechies, I.: 1988, 'Orthonormal Bases of Compactly Supported Wavelets', *Comm. Pure Appl. Math.* **41**, 909–996.

Deardorff, J. W. and Willis, G. E.: 1984, 'Ground-level Concentration Fluctuations From a Buoyant and Non-buoyant Source within a Laboratory Convective Mixed Layer', *Atmos. Environ.* **18**, 1297–1309.

Dinar, N., Kaplan, H., and Kleiman, M.: 1988, 'Characterization of Concentration Fluctuations of a Surface Plume in a Neutral Boundary Layer', *Boundary-Layer Meteorol.* **45**, 157–175.

Everson, R., Sirovich, L., and Sreenivasan, K. R.: 1990, 'Wavelet Analysis of the Turbulent Jet', *Phys. Lett. A* **145**, 314–322.

Fackrell, J. E. and Robins, A. G.: 1982, 'Concentration Fluctuations and Fluxes in Plumes from Point Sources in a Turbulent Boundary Layer', *J. Fluid Mech.* **117**, 1–26.

Farge, M.: 1992, 'Wavelet Transforms and Their Applications to Turbulence', *Annu. Rev. Fluid Mech.* **24**, 395–457.

Gao, W. and Li, B. L.: 1993, 'Wavelet Analysis of Coherent Structures at the Atmospheric-Forest Interface', *J. Appl. Meteorol.* **32**, 1717–1725.

Hanna, S. R.: 1984, 'The Exponential Probability Density Function and Concentration Fluctuations in Smoke Plumes', *Boundary-Layer Meteorol.* **29**, 361–375.

Hanna, S. R. and Insley, E. M.: 1989, 'Time Series Analysis of Concentration and Wind Fluctuations', *Boundary-Layer Meteorol.* **47**, 131–147.

Hayashi, T.: 1994, 'An Analysis of Wind Velocity Fluctuations in the Atmospheric Surface Layer using an Orthornormal Wavelet Transform', *Boundary-Layer Meteorol.* **70**, 307–326.

Katul, G. G., Parlange, M. B., and Chu, C. R.: 1994, 'Intermittency, Local Isotropy, and Non-Gaussian Statistics in Atmospheric Surface Layer Turbulence', *Phys. Fluids* **6**, 2480–2492.

Kumar, P. and Foufoula-Georgiou, E.: 1993, 'A New Look at Rainfall Fluctuations and Scaling Properties of Spatial Rainfall using Orthogonal Wavelets', *J. Appl. Meteorol.* **32**, 1993.

Lovejoy, S. and Schertzer, D.: 1985, 'Generalized Scale Invariance in the Atmosphere and Fractal Models of Rain', *Water Resour. Res.* **21**, 1233–1250.

Mahrt, L.: 1991, 'Eddy Asymmetry in the Shear Heated Boundary Layer', *J. Atmos. Sci.* **48**, 472–492.

Mallat, S.: 1989, 'A Theory for Multiresolution Signal Decomposition: The Wavelet Representation', *IEEE Trans. Pattern Anal. and Machine Intell.* **11**, 674–693.

Meneveau, C.: 1991, 'Analysis of Turbulence in the Orthonormal Wavelet Representation', *J. Fluid Mech.* **232**, 469–520.

Mylne, K. R.: 1993, 'The Vertical Profile of Concentration Fluctuations in Near-Surface Plumes', *Boundary-Layer Meteorol.* **65**, 111–136.

Mylne, K. R. and Mason, P. J.: 1991, 'Concentration Fluctuation Measurements in a Dispersing Plume at a Range of up to 1000 m', *Quart. J. Roy. Meteorol. Soc.* **117**, 177–206.

Peterson, H., Lamb, B., and Stock, D.: 1990, 'Interpretation of Measured Tracer Concentration Fluctuations using a Sinsusoid Meandering Plume Model', *J. Appl. Meteorol.* **29**, 1284–1299.

Sawford, B. L., Frost, C. C., and Allan, T. C.: 1985, 'Atmospheric Boundary-Layer Measurements of Concentration Statistics from Isolated and Multiple Sources', *Boundary-Layer Meteorol.* **31**, 249–268.

Silverman, B. W.: 1982, 'Kernel Density Estimation using Fast Fourier Transform', *Applied Statistics* **31**, 93–99.

Stapountzis, H., Sawford, B. L., Hunt, J. C. R., and Britter, R. E.: 1986, 'Structure of the Temperature Field Downwind of a Line Source in Grid Turbulence', *J. Fluid Mech.* **165**, 401–424.

Taswell, C. and McGill, K. C.: 1994, 'Algorithm 735: Wavelet Transform Algorithms for Finite-Duration Discrete-Time Signals', *ACM Trans. Math. Software* **20**, 398–412.

Terrell, G. R.: 1990, 'The Maximal Smoothing Principle in Density Estimation', *J. Amer. Statist. Assoc.* **85**, 470–477.

Townsend, A. A.: 1959, 'Temperature Fluctuations Over a Heated Horizontal Surface', *J. Fluid Mech.* **5**, 209–241.

Vainshtein, S. I., Sreenivasan, K. R., Pierrehumbert, R. T., Kashyap, V., and Juneja, A.: 1994, 'Scaling Exponents for Turbulence and Other Random Processes and Their Relationships with Multifractal Structure', *Phys. Rev. E* **50**, 1823–1835.

Vergassola, M. and Frisch, U.: 1991, 'Wavelet Transforms of Self-Similar Processes', *Physica D* **54**, 58–64.

Warhaft, Z.: 1984, 'The Interference of Thermal Fields from Line Sources in Grid Turbulence', *J. Fluid Mech.* **144**, 363–387.

Yamada, M. and Ohkitani, K.: 1991, 'An Identification of Energy Cascade in Turbulence by Orthonormal Wavelet Analysis', *Prog. Theor. Phys.* **86**, 799–815.

Yamada, M. and Ohkitani, K.: 1990, 'Orthonormal Wavelet Expansion and Its Application to Turbulence', *Prog. Theor. Phys.* **83**, 819–823.

Yee, E., Chan, R., Kosteniuk, P. R., Chandler, G. M., Biltoft, C. A., and Bowers, J. F.: 1995, 'The Vertical Structure of Concentration Fluctuation Statistics in Plumes Dispersing in the Atmospheric Surface Layer', *Boundary-Layer Meteorol.* **76**, 41–67.

Yee, E., Chan, R., Kosteniuk, P. R., Chandler, G. M., Biltoft, C. A., and Bowers, J. F.: 1994a, 'Experimental Measurements of Concentration Fluctuations and Scales in a Dispersing Plume in the Atmospheric Surface Layer Obtained using a Very Fast-Response Concentration Detector', *J. Appl. Meteorol.* **33**, 996–1016.

Yee, E., Chan, R., Kosteniuk, P. R., Chandler, G. M., Biltoft, C. A., and Bowers, J. F.: 1994b, 'Concentration Fluctuation Measurements in Clouds Released from a Quasi-Instantaneous Point Source in the Atmospheric Surface Layer', *Boundary-Layer Meteorol.* **71**, 341–373.

Yee, E., Kosteniuk, P. R., Chandler, G. M., Biltoft, C. A., and Bowers, J. F.: 1993, 'Statistical Characteristics of Concentration Fluctuations in Dispersing Plumes in the Atmospheric Surface Layer', *Boundary-Layer Meteorol.* **65**, 69–109.